

Predicting Frictional Properties of Graphene Kirigami Using Molecular Dynamics and Neural Networks

Designs for a negative friction coefficient.

Mikkel Metzsch Jensen



Thesis submitted for the degree of
Master in Computational Science: Materials Science
60 credits

Department of Physics
Faculty of mathematics and natural sciences

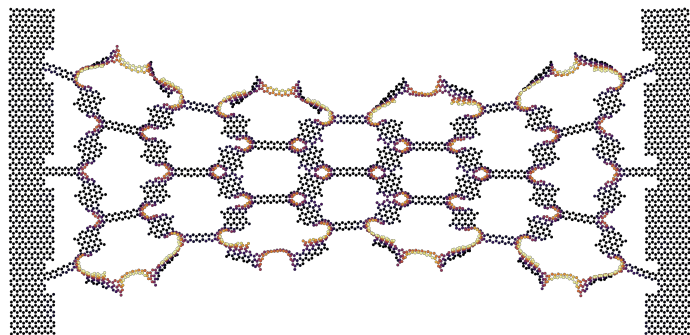
UNIVERSITY OF OSLO

Spring 2023

Predicting Frictional Properties of Graphene Kirigami Using Molecular Dynamics and Neural Networks

Designs for a negative friction coefficient.

Mikkel Metzsch Jensen



© 2023 Mikkel Metzsch Jensen

Predicting Frictional Properties of Graphene Kirigami Using Molecular Dynamics and Neural Networks

<http://www.duo.uio.no/>

Printed: Reprocentralen, University of Oslo

Abstract

Abstract.

Acknowledgments

Acknowledgments.

List of Symbols

F_N Normal force (normal load)

Acronyms

AFM Atomic Force microscope. 21, 22, 23, 25

CM Center of Mass. 34, 35

FFM Friction Force Microscopes. 21, 22, 23, 24, 25

FK Frenkel-Kontorova. 11, 16, 17, 18, 19, 20, 23, 24

FKT Frenkel-Kontorova–Tomlinson. 11, 20, 23, 24

GS Ground State. 17, 18

LJ Lennard-Jones. 39, 54

MD Molecular Dynamics. 1, 2, 3, 10, 11, 12, 14, 23, 24, 25, 26, 29, 30, 33, 41, 44, 51, 52, 53

ML Machine Learning. 2, 3, 30, 53

PT Prandtl–Tomlinson. 11, 16, 17, 19, 20, 22, 23, 25

SFA Surface force apparatus. 22, 23

SFM Scanning Force Microscopies. 21

SPM Scanning Probe Microscopy. 21

std Standard Deviation. 36, 37, 40, 42

Contents

1	Introduction	1
1.1	Motivation	1
1.2	Goals	2
1.3	Contributions	3
1.4	Thesis structure	3
I	Background Theory	5
2	Friction	7
2.1	Friction across scales	7
2.2	Macroscale	7
2.2.1	Amontons' law	7
2.3	Microscopic scale	9
2.3.1	Asperity theories	9
2.4	Nanoscale — Atomic scale	10
2.4.1	Prandtl–Tomlinson	11
2.4.1.1	Thermal activation	12
2.4.1.2	Sliding speed	14
2.4.1.3	Tip mass	15
2.4.1.4	Friction Regimes: Smooth Sliding, Single Slip, and Multiple Slip	15
2.4.2	Frenkel-Kontorova	16
2.4.2.1	Commensurability	17
2.4.2.2	Velocity resonance	19
2.4.3	Frenkel-Kontorova-Tomlinson	20
2.4.4	Shortcomings of atomic models	21
2.4.5	Experimental procedures	21
2.4.5.1	Scanning Probe Microscopy	21
2.4.5.2	Surface Force Apparatus	22
2.5	Summary of previous results	22
2.6	Research questions	25
II	Simulations	27
3	Pilot study	29
3.1	Friction simulation parameters	29
3.2	Force traces	30
3.2.1	Force oscillations	30
3.2.2	Decompositions	34
3.2.3	Center of mass path	34
3.3	Defining metrics for friction	36
3.3.1	Kinetic friction	36
3.3.2	Static friction	37

3.4	Out-of-plane buckling	38
3.5	Investigating default parameters	40
3.5.1	Computational cost	42
3.6	Load and stretch dependencies	44
3.6.1	Pressure reference for normal load	44
3.6.2	Strain dependency	44
3.6.3	Load dependency	47
3.6.4	Prospects of a negative friction coefficient	48
4	Summary	51
4.1	Summary and conclusions	51
4.1.1	Designing an MD simulation	51
4.1.2	Generetig Kirigami patterns	52
4.1.3	Control friction using Kirigami	52
4.1.4	Capture trends with ML	52
4.1.5	Accelerated search	53
4.1.6	Negative friction coefficient	54
4.2	Outlook / Perspective	54
Appendices		55
A	Appendix A	57
A	Appendix B	59
B	Appendix C	61

Chapter 1

Introduction

1.1 Motivation

Friction is the force that prevents the relative motion of objects in contact. Even though the everyday person might not be familiar with the term *friction* we recognize it as the inherent resistance to sliding motion. Some surfaces appear slippery and some rough, and we know intuitively that sliding down a snow-covered hill is much more exciting than its grassy counterpart. Without friction, it would not be possible to walk across a flat surface, lean against the wall without falling over or secure an object by the use of nails or screws [p. 5] [1]. It is probably safe to say that the concept of friction is integrated into our everyday life to such an extent that most people take it for granted. However, the efforts to control friction date back to the early civilization (3500 B.C.) with the use of the wheel and lubricants to reduce friction in translational motion [2]. Today, friction is considered a part of the wider field *tribology* derived from the Greek word *Tribos* meaning “rubbing” and includes the science of friction, wear and lubrication [2]. The most compelling motivation to study tribology is ultimately to gain full control of friction and wear for various technical applications. Especially, reducing friction is of great interest as this has tremendous advantages for energy efficiency. It has been reported that tribological problems have a significant potential for economic and environmental improvements [3]:

“On global scale, these savings would amount to 1.4% of the GDP annually and 8.7% of the total energy consumption in the long term.” [4].

On the other hand, the reduction of friction is not the only sensible application for tribological studies. Controlling frictional properties, besides minimization, might be of interest in the development of a grasping robot where finetuned object handling is required. While achieving a certain “constant” friction response is readily obtained through appropriate material choices, we are yet to unlock the full capabilities to alter friction dynamically on the go. One example from nature inspiring us to think along these lines are the gecko feet. More precisely, the Tokay gecko has received a lot of attention in scientific studies aiming to unravel the underlying mechanism of its “toggable” adhesion properties. Although geckos can produce large adhesive forces, they retain the ability to remove their feet from an attachment surface at will [5]. This makes the gecko able to achieve a high adhesion on the feet when climbing a vertical surface while lifting them for the next step remains relatively effortless. For a grasping robot, we might consider an analog frictional concept of a surface material that can change from slippery to rough on demand depending on specific tasks; Slippery and smooth when interacting with people and rough and firmly gripping when moving heavy objects.

In recent years an increasing amount of interest has gone into the studies of the microscopic origin of friction, due to the increased possibilities in surface preparation and the development of nanoscale experimental methods. Nano-friction is also of great concern for the field of nano-machining where the frictional properties between the tool and the workpiece dictate machining characteristics [3]. With concurrent progress in computational capacity and development of Molecular Dynamics (MD), numerical investigations serve as an invaluable tool for getting insight into the nanoscale mechanics associated with friction. This simulation-based approach can be considered as a “numerical experiment” enabling us to create and probe a variety of high-complexity systems which are still out of reach for modern experimental methods.

In materials science such MD-based numerical studies have been used to explore the concept of so-called *metamaterials* where material compositions are designed meticulously to enhance certain physical properties [6–

[11]. This is often achieved either by intertwining different material types or removing certain regions completely. In recent papers by Hanakata et al. [6, 7] numerical studies have showcased that the mechanical properties of a graphene sheet, yield stress and yield strain, can be altered through the introduction of so-called *kirigami* inspired cuts into the sheet. Kirigami is a variation of origami where the paper is cut additionally to being folded. While these methods originate as an art form, aiming to produce various artistic objects, they have proven to be applicable in a wide range of fields such as optics, physics, biology, chemistry and engineering [12]. Various forms of stimuli enable direct 2D to 3D transformations through folding, bending, and twisting of microstructures. While original human designs have contributed to specific scientific applications in the past, the future of this field is highly driven by the question of how to generate new designs optimized for certain physical properties. However, the complexity of such systems and the associated design space make for seemingly intractable problems ruling out analytic solutions.

Earlier architecture design approaches such as bioinspiration, looking at gecko feet for instance, and Edisonian, based on trial and error, generally rely on prior knowledge and an experienced designer [9]. While the Edisonian approach is certainly more feasible through numerical studies than real-world experiments, the number of combinations in the design space rather quickly becomes too large for a systematic search, even when considering the computation time on modern-day hardware. However, this computational time constraint can be relaxed by the use of machine learning (ML) which has proven successful in the establishment of a mapping from the design space to physical properties of interest. This gives rise to two new styles of design approaches: One, by utilizing the prediction from a trained network we can skip the MD simulations altogether resulting in an *accelerated search* of designs. This can be further improved by guiding the search accordingly to the most promising candidates, for instance, as done with the *genetic algorithm* based on mutation and crossing of the best candidates so far. Another more sophisticated approach is through generative methods such as *Generative Adversarial Networks* (GAN) or diffusion models with the latter being used in state-of-the-art AI systems such as OpenAI's DALL-E2 or Midjourney [SOURCE?](#). By working with a so-called *encoder-decoder* network structure, one can build a model that reverses the prediction process. That is, the model predicts a design from a set of physical target properties. In the papers by Hanakata et al both the *accelerated search* and the *inverse design* approach was proven successful to create novel metamaterial kirigami designs with the graphene sheet.

Hanakata et al attribute the variety in yield properties to the non-linear effects arising from the out-of-plane buckling of the sheet. Since it is generally accepted that the surface roughness is of great importance for frictional properties it can be hypothesized that Kirigami-induced out-of-plane buckling can also be exploited for the design of frictional metamaterials. For certain designs, we might hope to find a relationship between the stretching of the sheet and frictional properties. If significant, this could give rise to an adjustable friction behavior beyond the point of manufacturing. For instance, the grasping robot might apply such a material as artificial skin for which stretching or relaxing of the surface could result in a changeable friction strength.

In addition, the Kirigami graphene properties can be explored through a potential coupling between the stretch and the normal load, through a nanomachine design, with the aim of altering the friction coefficient. This invites the idea of non-linear friction coefficients which might in theory also take on negative values. The latter would constitute a rarely found property which is mainly found for the unloading phase of adhesive surfaces [13] or for the loading phase of particular heterojunction materials [14, 15].

To the best of our knowledge, Kirigami has not yet been implemented to alter the frictional properties of a nanoscale system. However, in a recent paper by Liefferink et al. [16] it is reported that macroscale kirigami can be used to dynamically control the macroscale roughness of a surface through stretching. They reported that the roughness change led to a changeable frictional coefficient by more than one order of magnitude. This supports the idea that Kirigami designs can be used to alter friction, but we believe that taking this concept to the nanoscale regime would involve a different set of underlying mechanisms and thus contribute to new insight in this field.

1.2 Goals

In this thesis, we investigate the possibility to alter the frictional properties of a graphene sheet through the application of Kirigami-inspired cuts and stretching of the sheet. With the use of molecular dynamics (MD) simulations, we evaluate the frictional properties of various Kirigami designs under different physical conditions. With the use of machine learning (ML), we perform an accelerated search of designs to explore new designs. The main goals of this thesis can be summarized as follows.

1. Design an MD simulation procedure to evaluate the frictional properties of a Kirigami graphene sheet under specified physical conditions.
2. Develop a numerical framework for creating various Kirigami designs, both by seeking inspiration from macroscale designs and by the use of a random walk based algorithm.
3. Investigate the frictional behavior under varying load and stretch for different Kirigami designs.
4. Develop and train an ML model to predict the MD simulation result and perform an accelerated search of new designs for the scope of optimizing certain frictional properties.

1.3 Contributions

What did I actually achieve [Include Github link](#)

1.4 Thesis structure

In Part I: Background Theory, we cover the theoretical background related to Friction (Chapter 2), Molecular Dynamics (??) and Machine Learning (??).

In Chapter 2: Friction, we introduce the most relevant theoretical concepts of friction through a division by scale: Macroscale (Sec. 2.2), Microscale (Sec. 2.3) and nanoscale (Sec. 2.4). We emphasize the nanoscale since this is of the most importance for our study. This is followed by a summary of relevant experimental and numerical results Sec. 2.5 and a more formal specification of our research questions (Sec. 2.6).

In ??: Molecular Dynamics, we introduce the main concepts related to the simulations used in this thesis. The main parts involve a description of the potentials used (??), the numerical solutions (??) and the modeling of temperature (??)

In ??: Machine Learning, we introduce the basics of machine learning through a general presentation of the neural network ?? followed by the convolutional network (??) which we will use in our study. Additionally, we discuss a strategy for choosing model hypertuning (??) and a simple approach for model prediction explanations (). Finally, we introduce a version of the genetic algorithm applicable for accelerated search based on a machine learning model (??).

In Part II: Simulations, we define our numerical procedure and present and discuss the main findings of this thesis.

In ??: System, we ...

In ??: Pilot study, we ...

In ??: XXX ...

In ??: XXX, ...

The thesis is summarized in Chapter 4

Additional figures are shown in ??, ?? and ?? [get appendix with only letter A., B. and C.](#)

Part I

Background Theory

Chapter 2

Friction

Since we aim for controlling frictional properties, we will review the relevant theoretical understanding of friction in this chapter. We limit ourselves to the tribological subcategory, wearless dry friction, meaning that we consider friction in the absence of lubricant and wear between the contacting surfaces. We will direct the review towards our system of interest which will serve as a basis for a formal definition of our research questions.

2.1 Friction across scales

Tribological systems span a wide range of time and length scales, from geological stratum layers involved in earthquakes [3] to atomistic processes, such as the gliding motion of nanoclusters or nanomotors [17]. This vast difference in scale leads to different dominant frictional mechanisms. At the macroscale, systems are typically subject to relatively high loads and sliding speeds, resulting in significant contact stress and wear. On the other hand, the micro-/nanoscale regime occupies the opposite domain operating under a relatively small load and sliding speed with negligible wear [3] [2, p. 5]. While macroscale friction is often reduced into a few variables such as load, material type, sliding speed and surface roughness, it is clear that the micro-/nanoscale friction cannot be generalized under such a simple representation. On the micro-/nanoscale the tribological properties are dominated by surface properties which will yield a more complex behavior of said variables and introduce an additional sensitivity to variables such as temperature, humidity and even sliding history. The works of Bhushan and Kulkarni [18] showed that the friction coefficient decreased with scale even though the materials used were unchanged. This reveals an intrinsic relationship between friction and scale as the contact condition is altered.

The phenomenological descriptions of macroscale friction cannot yet be derived from the fundamental atomic principles, and bridging the gap between different length scales in tribological systems remains an open challenge [17]. Hence, the following sections will be organized into macroscale (Sec. 2.2), microscale (Sec. 2.3) and nanoscale (Sec. 2.4) representing the theoretical understanding governing each scale regime. Realizing that the field of friction across all scales is a vastly broad topic, we will only introduce the most essential findings for each scale, while keeping a main focus on features associated with our system which takes place at the nanoscale.

2.2 Macroscale

Our working definition of the *macroscale* is everything on the scale of millimeters and above [19]. This represents the scale of visible objects and includes everything from the everyday interaction with an object to the geological systems.

2.2.1 Amontons' law

In order to start and keep a solid block moving against a solid surface we must overcome certain frictional forces F_{fric} [1]. The static friction force F_s corresponds to the minimum tangential force required to initiate the sliding while the kinetic friction force F_k corresponds to the tangential force needed to sustain such a sliding at a steady speed. The work of Leonardo da Vinci (1452–1519), Guillaume Amontons (1663–705) and Charles de Coulomb (1736–1806) all contributed to the empirical law, commonly known as *Amontons' law*, which serves as a common

base for macroscale friction. Amontons' law states that the frictional forces are entirely independent of contact area and sliding velocity. Instead, it relies only on the normal force F_N , acting perpendicular to the surface, and the material-specific friction coefficient μ as

$$F_{\text{fric}} = \mu F_N. \quad (2.1)$$

Notice that the term *normal force* is often used interchangeably with *load* and *normal load* although the load and normal load refer to the applied force that pushes the object into the surface, whereas the normal force is the reaction force acting from the surface on the object. In equilibrium, these forces are equal in magnitude and opposite in direction. and hence we will not make a distinction between these terms. On the same note, we point out that the frictional force is different from a conventional force which in the Newtonian definition acts on a body from the outside and makes it accelerate [20]. Rather than being an independent external force the friction force is an internal *reaction* force opposing the externally applied "sliding" force.

The friction coefficient μ is typically different for the cases of static (μ_s) and kinetic (μ_k) friction, usually both with values lower than one and $\mu_s \geq \mu_k$ in all cases [1, p. 6]. The friction coefficient is taken to be a constant defined by either [20]

$$\mu_1 = \frac{F_{\text{fric}}}{F_N}, \quad (2.2a) \quad \text{or} \quad \mu_2 = \frac{dF_{\text{fric}}}{dF_N}. \quad (2.2b)$$

The first definition Eq. (2.2a) requires zero friction at zero load, i.e. $F_{\text{fric}} = 0$ at $F_N = 0$, while the second definition Eq. (2.2b) allows for a finite friction force at zero load as the coefficient is defined by the slope of the $F_{\text{fric}}-F_N$ -curve. The consequences of these definitions are illustrated in Fig. 2.1, for selected $F_{\text{fric}}-F_N$ -curves in Fig. 2.1a and corresponding friction coefficients in Fig. 2.1b and Fig. 2.1c. For adhesive contacts, the friction force will not be zero under zero load (red curve: Linear + shift) which can be mitigated by adding an extra constant to Eq. (2.1) [20]. Using Eq. (2.2a) for adhesive contacts would make the friction coefficient diverge for decreasing load as illustrated in Fig. 2.1b. Thus, we find the second definition Eq. (2.2b) more robust and versatile. This also allows for a better interpretation of the friction coefficient in the case where friction depends non-linearly on load (Purple curve in Fig. 2.1).

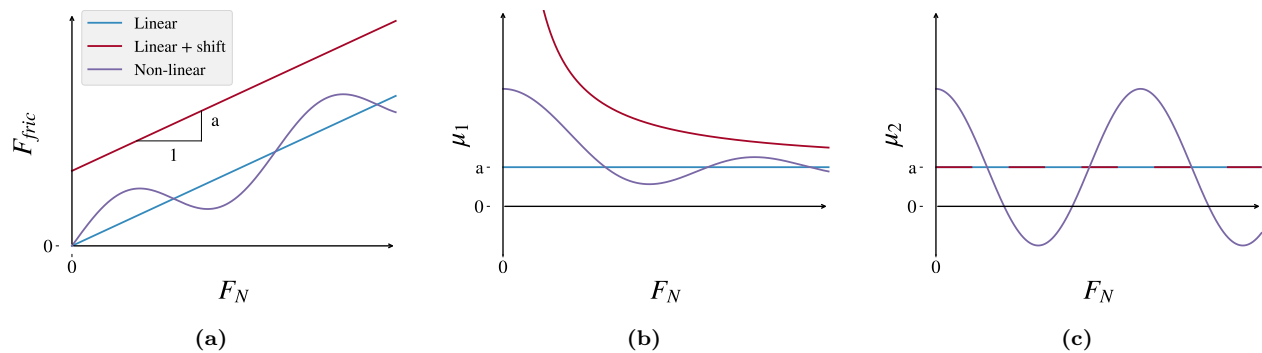


Figure 2.1: CAPTION

Amontons' law represents the behavior relatively accurately for many surfaces in contact, involving both dry and lubricated, ductile and brittle and rough and smooth surfaces (as long as they are not adhesive) under a variety of conditions [20]. But it has its limitations. For instance, at low velocities, Amontons' model breaks down due to thermal effects, and for high velocities due to inertial effects [1, pp. 5–6]. Additionally, static friction depends on the so-called contact history, with increasing static friction as the logarithm of time in stationary contact [21].

In cases where Amontons' law breaks down, we might still use the conceptual definition of the friction coefficient as defined by (Eq. (2.2b)). Especially, in the context of achieving negative friction coefficients (in certain load ranges), we would refer to this definition, since Eq. (2.2a) would imply a truly unphysical situation of the frictional force acting in the same direction as the sliding motion. This would accelerate the object indefinitely¹.

¹You would most likely have a good shot at the Nobel Prize with that paper.

Due to the empirical foundation of Amontons' law, it does not provide any physical insight into the underlying mechanisms of friction. However, as we will later discuss in more detail, we can understand the overall phenomena of friction through statistical mechanics by the concept of *equipartition of energy* [17]. A system in equilibrium has its kinetic energy uniformly distributed among all its degrees of freedom. When a macroscale object is sliding in a given direction it is clearly not in equilibrium since one of its degrees of freedom carries considerably more kinetic energy. Thus, the system will have a tendency to transfer kinetic energy to the remaining degrees of freedom in the form of heat dissipating to the surroundings and making the object slow down if not continuously driven forward by an external energy source. Hence, we can understand the overall concept of friction simply as the tendency of going toward equilibrium energy equipartitioning among many interacting degrees of freedom [17]. From this point of view, it is clear that friction is an inevitable part of contact physics, but even though friction cannot be removed altogether, we are still capable of manipulating it in useful ways.

The attentive reader might point out that we have already moved the discussion into the microscopic regime as *statistical mechanics* generally aim to explain macroscale behavior by microscopic interactions. In fact, this highlights the necessity to consider smaller scales in order to achieve a more fundamental understanding of friction.

We note that more advanced macroscale models for friction exist, for instance, the *earthquakelike* (EQ) model, also known as the *spring-and-block* model or the *multi-contact* model [Mani 2016] developed by Burridge and Knopoff [22]. This has been used in many studies of earthquake friction [23] and similar schemes have since been used to model the failure of fiber bundles and faults [24, 25]. Also, *rate and state* models have been used for earthquake modeling [26].

2.3 Microscopic scale

Going from a macro- to a microscale perspective, at a length scale on the order 10^{-6} m, it was realized that most surfaces are in fact rough [27]. The contact between two surfaces consists of numerous smaller contact points, so-called *asperities*, which form junctions due to contact pressure and adhesion as visualized in Fig. 2.2 [3]. In the macroscale perspective of Amonton's law, we refer to time- and space-averaged values, i.e. the apparent contact area and the average sliding speed [20]. However, microscopically we find the real contact area to be much smaller than the apparent area [3], and the shearing motion of local microjunctions to happen at large fluctuations rather than as one synchronized movement throughout the surface.

It is generally accepted that friction is caused by two mechanisms: Mechanical friction and chemical friction [3]. Mechanical friction is the “plowing” of the surface by hard particles or said asperities with an energy loss attributed to deformations of the asperity. While plastic deformations, corresponding to wear, gives rise to an obvious attribution for the energy loss, elastic deformations are also sufficient in explaining energy loss due to phonon excitations. The assumption of plastic deformations has been criticized as this is theorized only to be present at the beginning of a surface contact while it is negligible for prolonged or repeated contacts [28]. That is, when machine parts slide against each other for millions of cycles, the plastic deformation would only take place at the beginning for which the system then reaches a steady state with only elastic deformations. The chemical friction arises from adhesion between microscopic contacting surfaces, with an energy loss attributed to the breaking and forming of bonds. What kind of bonds

2.3.1 Asperity theories

Asperity theories have their foundations in the adhesion model proposed by Bowden and Tabor [29] which is based on the fundamental reasoning that friction is governed by the adhesion between two surfaces [30]. Adhesion is proportional to the real contact area defined by asperity junctions and interfacial shear strength τ between such contacting junctions. For an asperity contact area A_{asp} we get a true contact area $\sum A_{\text{asp}}$ leading to

$$F_{\text{fric}} = \tau \sum A_{\text{asp}}.$$

Note that this is still compatible with Amontons' law in Eq. (2.1) by having a linear relationship between the real contact area and the applied load. In fact, this is exactly how the theoretical model explains the friction dependency of load. By increasing the normal load it is hypothesized that the real contact area will increase as

the asperity tips are deformed (plastically or elastically) into broader contact points as visualized qualitatively in Fig. 2.2.

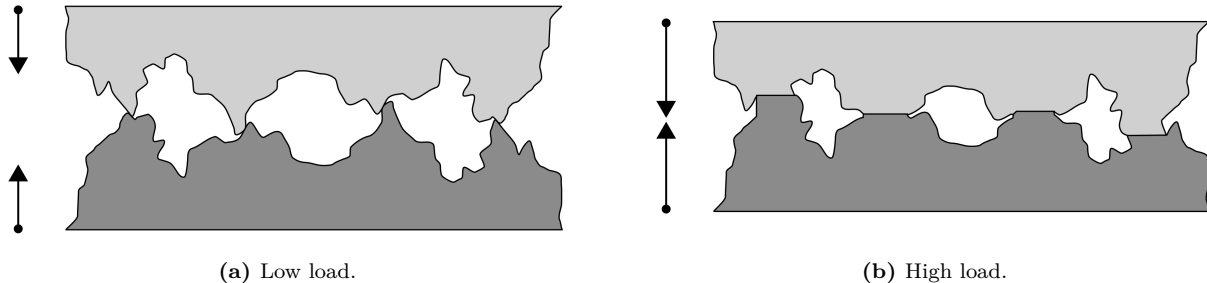


Figure 2.2: Qualitative illustration of the microscopic asperity deformation under increasing load from frame (a) to (b) [31]. While this figure seemingly portrays plastic deformation the concept of increased contact area under increased load applies to elastic deformation as well.

Many studies have focused on single asperity contacts to reveal the relationship between the contact area and load [32–34]. By assuming perfectly smooth asperities, with radii of curvature from micrometers all the way down to nanometers, continuum mechanics can be used to predict the deformation of asperities as load is applied. A model for non-adhesive contact between homogenous, isotropic, linear elastic spheres was first developed by Hertz [35], which predicted $A_{\text{asp}} \propto F_N^{2/3}$. Later adhesion effects were included in a number of subsequent models, including Maugis-Dugdale theory [36], which also predicts a sublinear relationship between A_{asp} and F_N . Thus, the common feature of all single-asperity theories is that A_{asp} is a sublinear function of F_N , leading to a similar sublinear relationship for $F_{\text{fric}}(F_N)$, which fails to align with the macroscale observations modeled by Amontons' law (eq. (2.1)).

Concurrently with single-asperity studies, roughness contact theories are being developed [37–40] to bridge the gap between single asperities and macroscopic contacts [27]. A variety of multi-asperity theories has attempted to combine single asperity mechanics by statistical modeling of the asperity height and spatial distributions [28]. This has led to partial success in the establishment of a linear relationship between A_{asp} and F_N . Unfortunately, these results are restricted in terms of the magnitude of the load and contact area, where multi-asperity contact models based on the original ideas of Greenwood and Williamson [39] only predicts linearity at vanishing low loads, or Persson [38] which predicts linearity for more reasonable loads but only up to 10–15 % of the macroscale contact area. However, as the load is further increased all multi-asperity models predict the contact area to fall into the sublinear dependency of normal force as seen for single asperity theories as well [28].

2.4 Nanoscale — Atomic scale

Going from a micro- to a nanoscale, on the order of 10^{-9} m, it has been predicted that continuum mechanics will start to break down [41] due to the discreteness of individual atoms. In a numerical MD study by Mo et al. [27], considering asperity radii of 5–30 nm, it has been shown that the asperity area A_{asp} , defined by the circumference of the contact zone, is sublinear with F_N . This is accommodated by the observation that not all atoms within the circumference make chemical contact with the substrate. By modeling the real contact area $A_{\text{real}} = N A_{\text{atom}}$, where N is the number of atoms within the range of chemical interaction and A_{atom} the associated surface area for a contacting atom, they found a consistent linear relationship between friction and the real contact area. Without adhesive forces, this leads to a similar linear relationship $F_{\text{fric}} \propto F_N$, while adding van der Waals adhesion to the simulation gave a sublinear relationship matching macroscale single asperity theory, even though the $F_{\text{fric}} \propto A_{\text{real}}$ was maintained. This result emphasizes that the predictions of continuum mechanics might still apply at the nanoscale and that the contact area can be expected to play an important role for nanoscale asperity contacts. It is simply the definition of the contact area that changes when transitioning from micro- to nanoscale.

While the study by Mo et al. [27] considers a single asperity on a nanoscale, some models take this even further to what we will denote as the atomic scale. This final leap is motivated by the fact that our system of interest, an atomically flat graphene sheet imposed on a flat silicon substrate, lacks the presence of nanoscale

asperities in its initial uncut undeformed state. In the lack of noteworthy structural asperities, friction can instead be modeled as a consequence of the “rough” potential laid out by the atomic landscape. A series of so-called *reduced-order* models build on a simplified system of atomic-scale contacts based on three essential parts: 1) A periodic potential modeling the substrate as a rigid crystalline surface. 2) An interacting particle, or collection of particles, placed in the potential. 3) A moving body, moving at a steady speed, connected to the particles through a harmonic spring. In figure Fig. 2.3 three of the most common 1D models are displayed which we will address in the following sections. The time-honored Prandtl-Tomlinson (PT) model describes a point-like tip sliding over a space-periodic fixed crystalline surface with a harmonic coupling to the moving body. This is analog to that of an experimental cantilever used for Atomic Force Microscopy which we will introduce in more detail in Sec. 2.4.5.1. Further extensions were added in the Frenkel-Kontorova (FK) model by substituting the tip with a chain of harmonically coupled particles dragged from the end, and finally combined in the Frenkel-Kontorova-Tomlinson (FKT) with the addition of a more rigorous harmonic coupling between the moving body and each of the atoms in the chain. While these models cannot provide the same level of detail as atomistic simulations such as MD they enable investigation of atomic friction under most conditions, some of which are inaccessible to MD [42]. This makes these models an appropriate tool for investigating individual parameters and mechanisms governing friction.

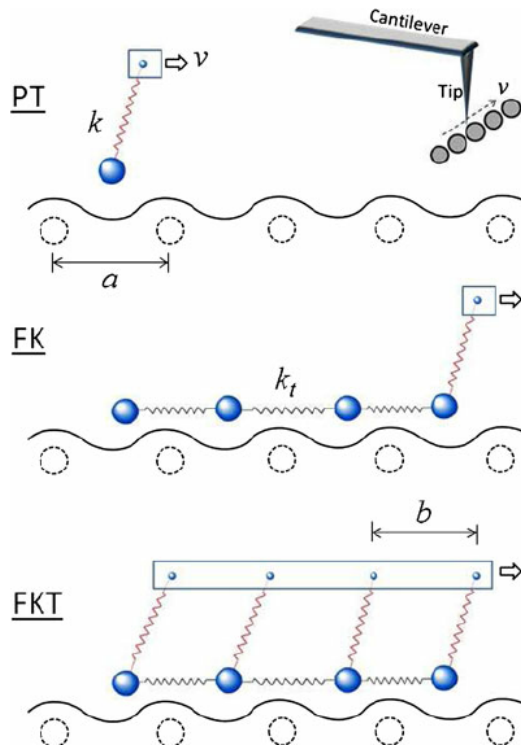


Figure 2.3: Temporary figure from [42]. Be careful to align the notation on the figures with the text later on.

2.4.1 Prandtl–Tomlinson

The Prandtl–Tomlinson model (PT) considers a 1D simplification of the frictional system as a single ball-tip sliding along the rigid substrate as shown in Fig. 2.3. The tip is coupled harmonically to a support moving at a constant speed which drives the tip forward. The interaction between the tip and the substrate is modeled as a sinusoidal corrugation potential mimicking the periodicity found in a crystalline substrate. We will consider Prandtl–Tomlinson model with added thermal activation as proposed by Gnecco et al. [43]. For the theoretical foundation of this section, we generally refer to [42]. The potential energy for the tip at position x for time t is given as

$$V(x, t) = \frac{1}{2}K(vt - x)^2 - \frac{1}{2}U_0 \cos\left(\frac{2\pi x}{a}\right). \quad (2.3)$$

The first term describes the harmonic coupling with spring constant K , between the tip at position x and the moving body at position vt , given by its constant speed v . The second term describes the corrugation potential with amplitude U_0 and period a representing the lattice spacing of the substrate. The dynamics of the tip can be described by the Langevin equations

$$m\ddot{x} + m\mu\dot{x} = -\frac{\partial V(x, t)}{\partial x} + \xi(t), \quad (2.4)$$

Match notation with later use.

where m is the mass of the tip, μ the viscous friction and $\xi(t)$ the thermal activation term. The equation is solved for tip position x and the friction force is retrieved as the force acting on the moving body

$$F_{\text{fric}} = K(vt - x).$$

The governing equation Eq. (2.4) belongs to a family of stochastic differential equations composed of both deterministic dynamics and stochastic processes. In this case, the deterministic term is the viscous friction, $m\mu\dot{x}$, to resist the movement of the tip and the force acting from the corrugation potential. The stochastic term is a random force field modeling thermal noise according to the Fluctuation-dissipation relation. Thus, there is no single path but rather multiple paths the tip can take. While the Langevin equations is one of the most common ways to handle thermal activation other methods exist to solve this problem such as Monte Carlo sampling methods. We omit the numerical scheme for the solving of the Langevin equations here and refer instead to a more in-depth discussion of the Langevin equations regarding the MD simulations in ??.

2.4.1.1 Thermal activation

The solving of the Langevin equations, as opposed to Newton's equation of motion, introduces thermal effects to the system. Generally, when the energy barrier comes close to $k_B T$ (0.026 eV at room temperature) thermal effects can not be neglected. In the case of a single asperity contact the energy barrier is on the order 1 eV which makes thermal activation significant [42]. Due to the moving body traveling at a constant speed, the potential energy will increase steadily. Without any temperature, $T = 0$, the slip will only occur when the energy barrier between the current potential well (i) and the adjacent (j) is zero $\Delta V_{i \rightarrow j} = 0$. However, in the presence of temperature, we get thermal activation, meaning that the tip can slip to the next potential well sooner $\Delta V_{i \rightarrow j} > 0$. Provided that the sliding speed is slow enough (Elaborate) the transition rate κ for a slip from the current to the next well is given by

$$\kappa = f_0 e^{-\Delta V/k_B T}, \quad (2.5)$$

with ΔV being the energy barrier and f_0 the attempt rate. The attempt rate following Kramer's rate theory [44] is related to the mass and damping of the system and can be thought of as the frequency at which the tip "attempts" to overcome the barrier. Notice that Eq. (2.5) resembles a microstate probability in the canonical ensemble with f_0 in place of the inverse partition function Z^{-1} which provides an additional interpretation of f_0 . The probability p_i that the tip occupies the current well i relative to the adjacent well j , as illustrated in Fig. 2.4 is governed by

$$\frac{dp_i}{dt} = -\kappa_{i \rightarrow j} p_i + \kappa_{j \rightarrow i} p_j.$$

This probability is related to temperature, speed and mass [42].

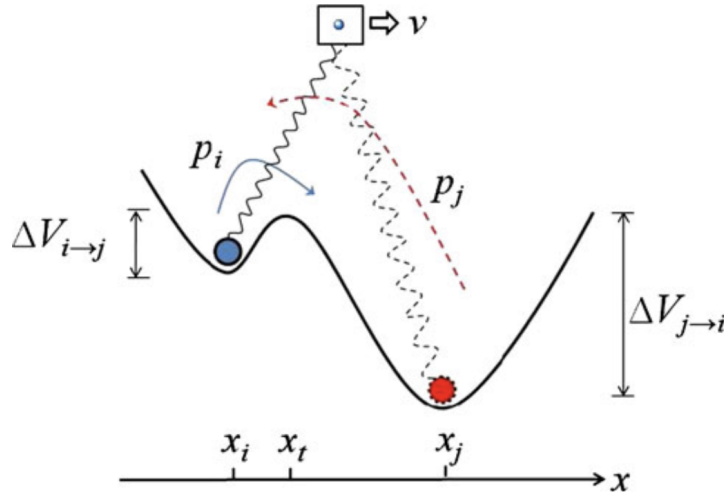


Fig. 3 An illustration of slip between two adjacent energy minima. p_i is the probability of the tip residing in the current potential well, i , where the energy barrier is $\Delta V_{i \rightarrow j}$. p_j is the probability of the tip residing at the next minima, j , where $\Delta V_{j \rightarrow i}$ is the corresponding energy barrier

Figure 2.4: [Temporary] figure from [42]

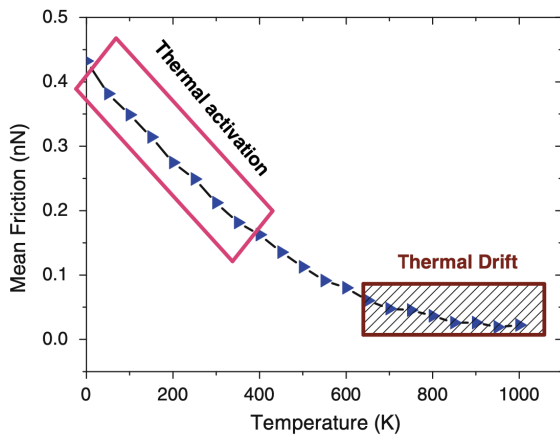
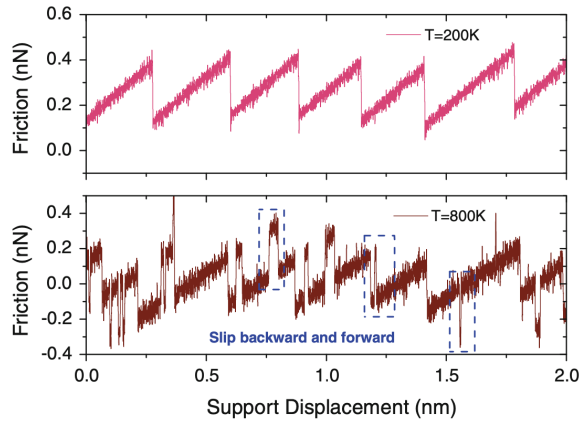


Fig. 4 Illustration of the temperature dependence of friction. The two regimes identified on the plot, thermal activation and thermal drift, are described in the text. Other model parameters: $m = 10^{-12}$ kg, $U = 0.6$ eV, $v = 4 \times 10^3$ nm/s, $\mu = 2\sqrt{k/m}$, $a = 0.288$ nm



(a)

(b)

Figure 2.5: [Temporary] figures from [42]

Generally, there exist two temperature regimes in the model: *Thermal activation* at low temperatures and *thermal drift* at high temperatures as shown in Fig. 2.5. At lower temperatures, the system is subject to standard thermal activation with $\Delta V_{j \rightarrow i} \gg \Delta V_{i \rightarrow j}$ resulting in $\kappa_{j \rightarrow i} \ll \kappa_{i \rightarrow j}$. Effectively, this inhibits any backward slip

and we get

$$\frac{dp_i}{dt} = -\kappa_{i \rightarrow j} p_i,$$

which makes the relationship between friction, temperature and speed follow Sang et al.'s prediction [45]

$$F = F_c - \left| \beta k_B T \ln \left(\frac{v_c}{v} \right) \right|^{2/3}, \quad v_c = \frac{2f_0 \beta k_B T}{3C_{\text{eff}} \sqrt{F_c}}, \quad (2.6)$$

where F_c is the maximum friction at $T = 0$, v_c a critical velocity, f_0 is the attempt rate, C_{eff} the effective stiffness, and β a parameter determined by the shape of the corrugation well. Eq. (2.6) characterizes the decrease in friction with temperature in the thermal activation regime, shown in Fig. 2.5a at low temperature. This corresponds with the assumption of only forward slips, as seen in the force trace shown in Fig. 2.5a. When the temperature is high enough for the system to be consistently close to thermal equilibrium, it enters the regime of thermal drift [46]. This regime transition can be understood through a comparison between two time scales: The time it takes for the moving body to travel one lattice spacing $t_v = a/v$ and the average time for a slip to occur due to thermal activation $\tau = 1/\kappa = f^{-1} \exp(\Delta V/k_B T)$. If $t_v \gg \tau$ the system falls within the thermal drift regime, with slips both backward and forwards as shown in Fig. 2.5b, and the friction follows the prediction of Krylov et al. [46–48]

$$F \propto \frac{v}{T} e^{1/T}. \quad (2.7)$$

Notice that the friction dependence on sliding speed changes between the temperature regimes as well.

2.4.1.2 Sliding speed

In the thermal activation regime (low temperature) and at low speeds the friction relation follows Eq. (2.6) making friction scale logarithmically with speed. For higher speed, above the critical velocity $v > v_c$, if only thermal effects are considered, Eq. (2.6) predicts that friction will eventually saturate and come to a plateau at $F_{\text{fric}} = F_c$. This is illustrated in Fig. 2.6 with this prediction being represented by the dotted line. However, as given away by the figure, for higher speed the model will enter an athermal regime where the thermal effects are negligible compared to other contributions [49]. In the athermal regime the damping term $m\mu\dot{x}$ will dominate yielding $F_{\text{fric}} \propto v$. The athermal regime is often observed in reduced-models if the system is overdamped or at high speeds. This concept is related to MD simulations where the accessible speeds often fall into the athermal regime [50]. It is unclear how this affects real physical systems for which there exist more dissipation channels than just a single viscous term [51]. For the thermal drift regime at higher temperatures the linear relation $F_{\text{fric}} \propto v$ as given by Eq. (2.7).

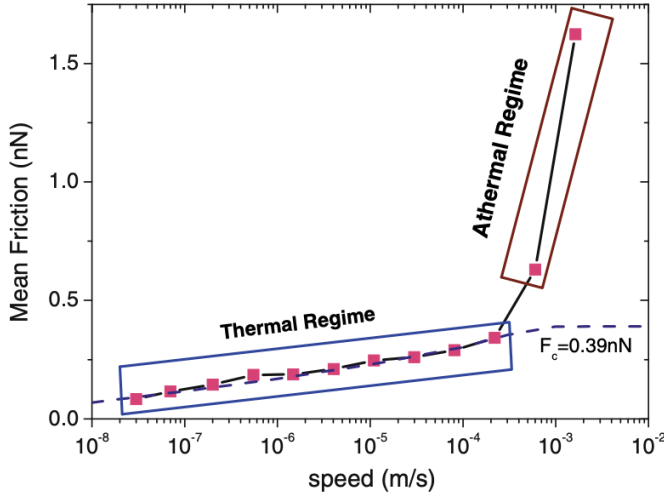


Fig. 6 Speed dependence of friction illustrating two different regimes. In the thermal regime, there is a logarithmic scaling of friction with speed, and in the athermal regime the friction is governed by the damping term such that $F \propto v$. The friction plateau ($F_c = 0.39$ nN) predicted by thermal activation is identified by the dashed line. Other model parameters: $m = 10^{-12}$ kg, $U = 0.6$ eV, $T = 300$ K, $v = 4 \times 10^3$ nm/s, $\mu = 2\sqrt{k/m}$, $a = 0.288$ nm

Figure 2.6: Temporary figure from [42]

2.4.1.3 Tip mass

The mass of the tip affects the dynamics due to a change of inertia, which changes the attempt rate f_0 . Smaller inertia leads to a larger attempt rate and vice versa. Effectively, this will affect the transition point for the temperature and speed regimes described previously. A smaller inertia, giving a larger attempt rate, will cause an earlier transition (i.e. at a lower temperature) to the thermal drift regime, and result in a later speed saturation such that it transitions to the athermal regime at a higher speed.

2.4.1.4 Friction Regimes: Smooth Sliding, Single Slip, and Multiple Slip

Stick-slip motion is a crucial instability mechanism associated with high energy dissipation and high friction. Thus, controlling the transition between smooth sliding and stick-slip is considered key to controlling friction. We can divide the frictional stick-slip behavior into three regimes: 1) Smooth sliding, where the tip slides smoothly on the substrate. 2) Single slip, where the tip sticks at one potential well before jumping one lattice spacing to the next. 3) Multiple slip, where the tip jumps more than one lattice spacing for a slip event. The underlying mechanisms behind these regimes can be understood through static and dynamic contributions.

To understand the static mechanism we consider a quasistatic process for which temperature, speed and damping can be neglected and where we must have $\partial(V)/\partial x = 0$. This simplifies Eq. (2.3) to

$$\frac{\pi U_0}{a} \sin\left(\frac{2\pi x}{a}\right) \frac{2\pi}{a} = K(vt - x). \quad (2.8)$$

The friction regime is determined by the number of solutions x to Eq. (2.8). Only one solution corresponds to smooth sliding, two solutions to a single slip and so on. It turns out that the regimes can be defined by the parameter $\eta = 2\pi^2 U_0/a^2 K$ [52, 53] yielding transitions at $\eta = 1, 4.6, 7.79, 10.95, \dots$, such that $\eta \leq 1$ corresponds to smooth sliding, $1 < \eta \leq 4.6$ to a single slip and so on. These static derivations lay out the fundamental probabilities for being in one of the stick-slip regimes. Notice that increasing the spring constant K (stiff spring) will decrease the possibilities for stick-slip behavior. Similarly, the potential corrugation U_0 can be altered through an increased load of the system U_0 can be altered by an increasing load [54]

Considering the dynamics on top, one finds that damping, speed and temperature will affect this probability. High damping, equivalent to a high transfer of kinetic energy to heat, will result in less energy available for the slip events. This will make multiple slip less likely. By a similar argument, we find that increasing the speed will contribute to more kinetic energy which will increase the likelihood of multiple slip. Finally, the temperature will contribute to earlier slips, due to thermal activation, such that less potential energy can be accumulated and it will result in fewer multiple slip. The effects of damping, speed and temperature are illustrated for the force traces in Fig. 2.7

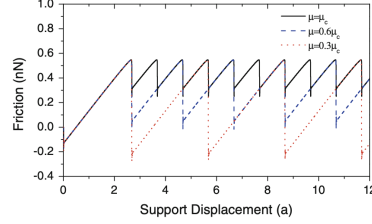


Fig. 9 The effect of damping on transitions between slip regimes where $\mu_c = 2\sqrt{k/m}$ is the critical damping coefficient. Single, double, and triple slip occur at $\mu = \mu_c$, $0.6 \mu_c$, and $0.3 \mu_c$, respectively. The abscissa has units of the lattice spacing a to facilitate identification of the transitions between single, double, and triple regimes. Other model parameters: $U = 0.6 \text{ eV}$, $T = 0 \text{ K}$, $v = 1 \mu\text{m/s}$, $m = 10^{-12} \text{ kg}$, $k = 1 \text{ N/m}$, $a = 0.288 \text{ nm}$

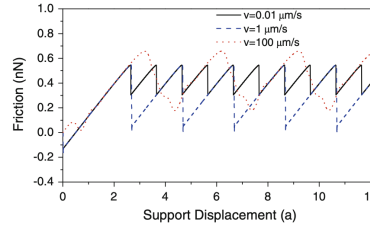


Fig. 10 The effect of sliding speed on transitions between slip regimes. Single, double, and triple slip occur at $v = 100$, 1 , and $0.01 \mu\text{m/s}$, respectively. Other model parameters: $U = 0.6 \text{ eV}$, $T = 0 \text{ K}$, $\mu = 0.8 \mu_c$, $m = 10^{-12} \text{ kg}$, $k = 1 \text{ N/m}$, $a = 0.288 \text{ nm}$

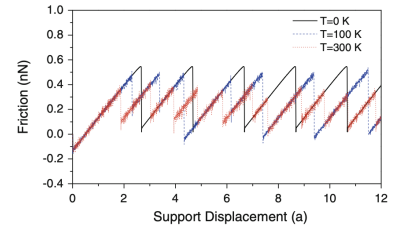


Fig. 11 The effect of temperature on transitions between slip regimes. Other model parameters: $U = 0.6 \text{ eV}$, $v = 1 \mu\text{m/s}$, $\mu = 0.6 \mu_c$, $m = 10^{-12} \text{ kg}$, $k = 1 \text{ N/m}$, $a = 0.288 \text{ nm}$

(a)

(b)

(c)

Figure 2.7: Temporary figure from [42]. Consider removing since the interpretation of smooth sliding might get a bit tricky.

2.4.2 Frenkel-Kontorova

The Frenkel-Kontorova (FK) model [55] extends the PT model by considering a chain of atoms in contrast to just a single particle (tip). This extension is useful for understanding the importance of the alignment between the atoms and the substrate, the so-called *commensurability*.

The standard (FK) model consists of a 1D chain of N classical particles of equal mass, representing atoms, interacting via harmonic forces and moving in a sinusoidal potential as sketched in Fig. 2.8 [17]. The Hamiltonian is

$$H = \sum_{i=1}^N \left[\frac{p_i^2}{2m} + \frac{1}{2}K(x_{i+1} - x_i - a_c)^2 + \frac{1}{2}U_0 \cos\left(\frac{2\pi x_i}{a_b}\right) \right], \quad (2.9)$$

where the atoms are labelled sequentially $i = 1, \dots, N$. The first term $p_i^2/2m$ represents the kinetic energy with momentum p_i and mass m . Often the effects of inertia are neglected, referred to as the static FK model, while the inclusion in Eq. (2.9) is known as the dynamic FK model [56]. The next term describes the harmonic interaction with elastic constant K , nearest neighbour distance $\Delta x = x_{i+1} - x_i$ and corresponding nearest neighbour equilibrium distance a_c . The final term represents the periodic corrugation potential, with amplitude U_0 and period a_b . By comparison to the potential used in the PT model Eq. (2.3), the only difference is the introduction of a harmonic coupling between particles in the chain as opposed to the moving body, and that we have not yet specified any force incentivizing sliding. Different boundary choices can be made where both free ends and periodic conditions give similar results. The choice of fixed ends however makes the chain incapable of sliding.

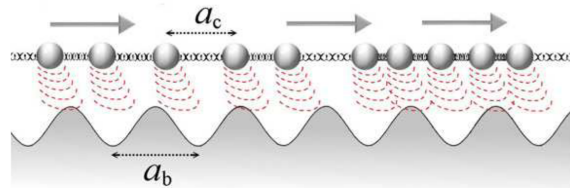


Figure 1. A sketch of the FK model, showing the two competing lengths: the average interparticle spacing and the lattice periodicity of the substrate.

Figure 2.8: Temporary figure from [17]

To probe static friction one can apply an external adiabatically increasing force until sliding occurs. This corresponds to the static FK model, and it turns out that the sliding properties are entirely governed by its topological excitations referred to as so-called *kinks* and *antikinks*

2.4.2.1 Commensurability

We can subdivide the frictional behavior in terms of commensurability, that is, how well the spacing of the atoms matches the periodic substrate potential. We describe this by the length ratio $\theta = a_b/a_c = N/M$ where M denotes the number of minima in the potential (within the length of the chain). A rational number for θ means that we can achieve a perfect alignment between the atoms in the chain and the potential minima, without stretching the chain, corresponding to a *commensurate* case. If θ is irrational the chain and substrate cannot fully align without some stretching of the chain, and we denote this as being *incommensurate*.

We begin with the simplest commensurate case of $\theta = 1$ where the spacing of the atoms matches perfectly with the substrate potential periodicity, i.e. $a_c = a_b$, $N = M$. The ground state (GS) is the configuration where each atom is aligned with one of the substrate minima. By adding an extra atom to the chain we would effectively shift some of the atoms, out of this ideal state, giving rise to a kink excitation. This leads to the case where two atoms will have to “share” the same potential corrugation as sketched in Fig. 2.10. On the other hand, removing an atom from the chain results in an antikink excitation where one potential corrugation will be left “atomless”. In order to reach a local minimum the kink (antikink) will expand in space over a finite length such that the chain undertakes a local compression (expansion). Notice that for low ratios of θ , fewer atoms than minima, the chain will not be able to fill each corrugation well in any case, meaning that commensurability can instead be thought of as whether the atoms are forced to deviate, by a lattice spacing, from the spacing otherwise dictated by the spring forces in-between. When applying a tangential force to the chain it is much easier for an excitation to move along the chain than it is for the non-excited atoms since the activation energy ϵ_{PN} for a kink/antikink displacement is systematically smaller (often much smaller) than the potential barrier U_0 . Thus, the motion of kinks (antikinks), i.e. the displacement of extra atoms (atom vacancies), is representing the fundamental mechanism for mass transport. These displacements are responsible for the mobility, diffusivity and conductivity within this model.

In the zero temperature commensurable case with an adiabatical increase in force, all atoms would be put into an accelerating motion as soon as the potential barrier energy is present. However, just as discussed for the PT model, thermal activations will excite the system at an earlier stage resulting in kink-antikink pairs traveling down the chain. For a chain of finite length, these often occur at the end of the chain running in opposite directions. This cascade of kink-antikink excitations is shown in Fig. 2.9. Notice, that for the 2D case, where an island (or flake) is deposited on a surface, we generally also expect the sliding to be initiated by kink-antikink pairs at the boundaries.

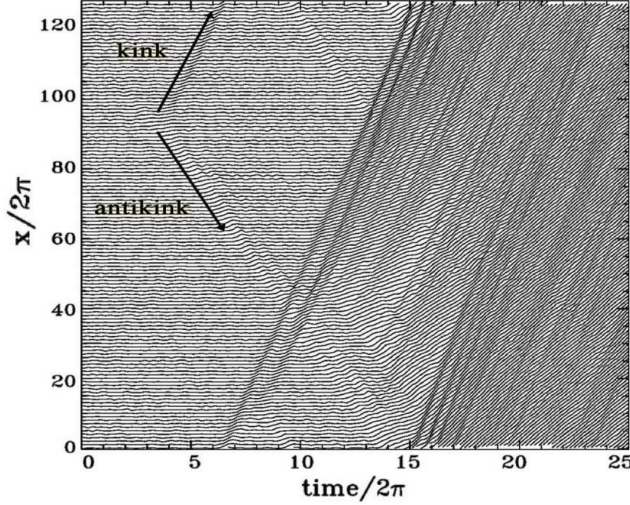


Figure 2. Time dependence of the atomic trajectories for the fully matched ($\theta = 1$) FK model at the (low-temperature) onset of depinning. Motion starts with the nucleation of a kink-antikink pair. The kink and the antikink depart in opposite directions cross the periodic boundary conditions, and collide quasielastically. A second kink-antikink pair forms in the wake of the initial kink. Further kink-antikink pairs are generated, with an avalanche-like increase of the kink-antikink concentration, eventually leading to a sliding state. Adapted from Ref. [21], Copyright (1997) by The American Physical Society.

Figure 2.9: Temporary figure from [17]

For the case of incommensurability, i.e. $\theta = a_b/a_c$ is irrational, the GS is characterized by a sort of “staircase” deformation. That is, the chain will exhibit regular periods of regions approximate commensurability separated by regularly spaced kinks or antikinks.



Figure 2.10: Temporary figure from [urlhttp://www.iop.kiev.ua/~obraun/myreprints/surveyfk.pdf](http://www.iop.kiev.ua/~obraun/myreprints/surveyfk.pdf) p. 14. Incommensurable case ($\theta = ?$) where atoms sit slightly closer than otherwise dictated by the substrate potential for which this regular result in a kink here seen as the presence of two atoms closely together in one of the potential corrugations.

The incommensurable FK model contains a critical elastic constant K_c , such that for $K > K_c$ the static friction F_s drops to zero, making the chain able to initiate a slide at no energy cost, while the low-velocity kinetic friction is dramatically reduced. This can be explained by the fact that the displacement occurring in the incommensurable case will yield just as many atoms climbing up a corrugation as there are atoms climbing down. For a big (infinite) chain this will exactly balance the forces making it non-resistant to sliding. Generally, incommensurability guarantees that the total energy (at $T = 0$) is independent of the relative position to the potential. However, when sliding freely, a single atom will eventually occupy a maximum of the potential, and thus when increasing the potential magnitude U_0 or softening the chain stiffness, lowering K , the possibility to occupy such a maximum disappears. This marks the so-called Aubry transition, at the critical elastic constant $K = K_c(U_0, \theta)$, where the chain goes from a free sliding to a *pinned* state with nonzero static friction. K_c is a discontinuous function of the ratio θ , due to the reliance on irrational numbers for incommensurability. The minimal value $K_c \simeq 1.0291926$ in units $[2U_0(\pi/a_b)^2]$ is achieved for the golden-mean ratio $\theta = (1 + \sqrt{5}/2)$. Notice that the pinning is provided despite translational invariance due to the inaccessibility to move past the energy

barrier which acts as a dynamical constraint. The Aubry transition can be investigated as a first-order phase transition for which power laws can be defined for the order parameter, but this is beyond the scope of this thesis.

The phenomena of non-pinned configurations are named *superlubricity* in tribological context. Despite the misleading name, this refers to the case where the static friction is zero while the kinetic friction is nonzero but reduced. For the case of a 2D sheet, it is possible to alter the commensurability, not only by changing the lattice spacing through material choice but also by changing the orientation of the sheet relative to the substrate. Dienwiebel et al. [57] have shown that the kinetic friction, for a graphene flake sliding over a graphite surface (multiple layers of graphene), exhibits extremely low friction at certain orientations as shown in Fig. 2.11. Here we clearly see that friction changes as a function of orientation angles with only two spikes of considerable friction force. This relates back to the concept of frictional regimes introduced through the simpler PT model, where the change in orientation affects the effective substrate potential. Merely from the static consideration, we found that lowering the potential amplitude U_0 will decrease the parameter $\eta = 2\pi^2 U_0/a^2 K$ shifting away from the regime of multiple slips towards smooth sliding associated with low friction. Such transitions will also be affected by the shape of the potential and corresponding 2D effects of the sliding path [42].

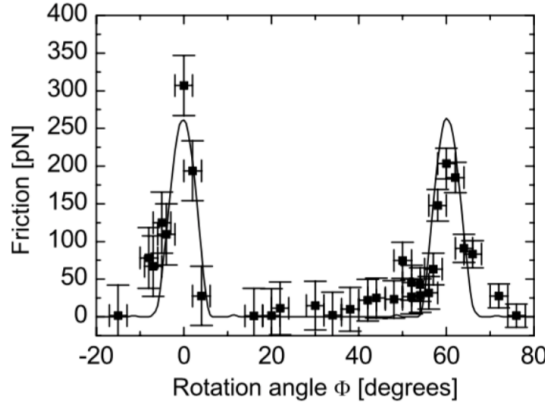


Fig. 6. Average friction force versus rotation angle Φ of the graphite sample around an axis normal to the sample surface. Two narrow peaks of high friction are observed at 0° and 61° , respectively. Between these peaks a wide angular range with ultra-low friction, close the detection limit of the instrument, is found. The first peak has a maximum friction force of 306 ± 40 pN, and the second peak has a maximum of 203 ± 20 pN. The curve through the data points shows results from a Tomlinson model for a symmetric 96-atom graphite flake sliding over the graphite surface (for details about the calculation see [39]).

Figure 2.11: **Temporary** figure from [57] showing superlubricity for incommensurable orientations between graphene and graphite. **temporary**

2.4.2.2 Velocity resonance

While many of the same arguments used for the PT model regarding velocity dependence for friction can be made for the FK model, the addition of multiple atoms introduces the possibility of resonance. In the FK model the kinetic friction is primarily attributed to resonance between the sliding induced vibrations and phonon modes in the chain [56]. The specific dynamics are found to be highly model and dimension specific, and even for the 1D case, this is rather complex. However, we make a simplified analysis of the 1D rigid chain case to showcase the reasoning behind the phenomena.

When all atoms are sliding rigidly with center of mass velocity v_{CM} the atoms will pass the potential maxima with the so-called *washboard frequency* $\Omega = 2\pi v_{CM}/ab$. For a weak coupling between the chain and the potential we can use the zero potential case as an approximation for which the known dispersion relation for the 1D

harmonic chain is given [58, p. 92]

$$\omega_k = \sqrt{\frac{4K}{m}} \left| \sin\left(\frac{k}{2}\right) \right|,$$

where ω_k is the phonon frequency and $k = 2\pi i/N$ the wavenumber with $i \in [N/2, N/2)$. Resonance will occur when the washboard frequency Ω is close to the frequency of the phonon modes ω_q in the chain with wavenumber $q = 2\pi a_c/a_b = 2\pi\theta^{-1}$ or its harmonics nq for $n = 1, 2, 3, \dots$ [59]. Thus, we can approximate the resonance center of mass speed as

$$\begin{aligned} n\Omega &\sim \omega_{nq} \\ n\frac{2\pi v_{CM}}{a_b} &\sim \sqrt{\frac{4K}{m}} \left| \sin\left(\frac{2n\pi\theta^{-1}}{2}\right) \right| \\ v_{CM} &\sim \frac{\sin(n\pi\theta^{-1})}{n\pi} \sqrt{\frac{Ka_b^2}{m}}. \end{aligned}$$

When the chain slides with a velocity around resonance speed, the washboard frequency can excite acoustic phonons which will dissipate to other phonon modes as well. At zero temperature, the energy will transform back and forth between internal degrees of freedom and center of mass movement of the chain. Without any dissipation mechanism this is theorized to speed up the translational decay [56]. However, as soon as we add a dissipation channel through the substrate, energy will dissipate from the chain to the substrate's degrees of freedom. This suggests that certain sliding speeds will exhibit relatively high kinetic friction while others will be subject to relatively low kinetic friction. Simulations of concentric nanotubes in relative motion (telescopic sliding) support this idea as it has revealed the occurrence of certain velocities at which the friction is enhanced, corresponding to the washboard frequency of the system [17], where the friction response was observed to be highly non-linear as the resonance velocities were approached.

The analysis of the phonon dynamics is highly simplified here, and a numerical study of the FK by Norell et al. [56] showed that the behavior was highly dependent on model parameter choices, but that the friction generally increased with velocity and temperature. Here the latter observation differs qualitatively from that of the PT model.

2.4.3 Frenkel-Kontorova-Tomlinson

A final extension of the atomic models worth mentioning here is the Frenkel-Kontorova-Tomlinson (FKT) model [60], which introduces a harmonic coupling of the sliding atom chain to the driving moving body, effectively combining PT and FK (see Fig. 2.3). This introduces more degrees of freedom to the model based on the intention of getting a more realistic connection between the moving body and the chain. Dong et al. carried out a numerical analysis using the 1D FKT model investigating the effect of chain length. They observed that the friction increased linearly with the number of atoms in the chain on a long-range, but certain lattice mismatch resulted in local non-linear relationships as shown in Sec. 2.4.3. Similarly, by extending the FKT model to 2D they were able to achieve a similar sensitivity to commensurability as observed experimentally by [57] (shown in Fig. 2.11) with the numerical result shown in Sec. 2.4.3. Besides a demonstration of the commensurability effect in 2D they also observed increasing friction with an increasing flake size. Combined, the 1D and 2D results support the idea of increasing friction with contact size although it might showcase non-linear behavior depending on commensurability.

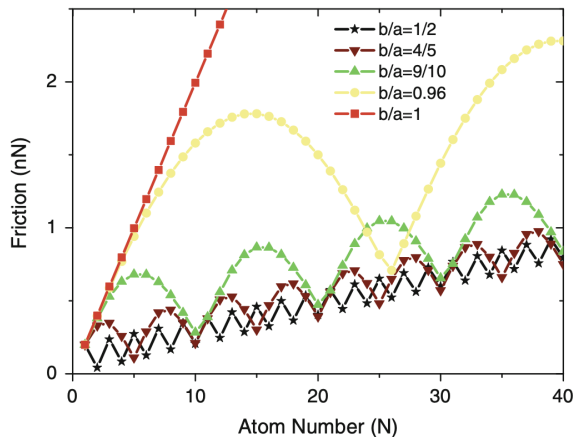


Fig. 21 Friction variation with the tip size N for different lattice mismatch b/a . $k = 5 \text{ N/m}$ and $k_t = 50 \text{ N/m}$ are used to obtain these results

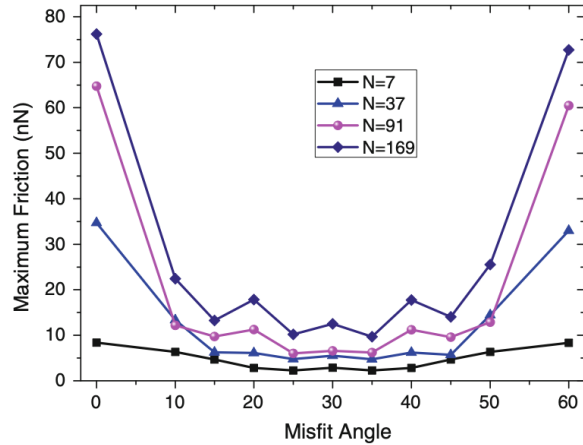


Fig. 23 The misfit angle dependence of friction with different tip sizes; $k_t = 50 \text{ N/m}$ and $k = 10 \text{ N/m}$. The $N = 7$ curve corresponds to the model illustrated in Fig. 22

(a) [Temporary] figure from [42]

(b) [Temporary] figure from [42]

2.4.4 Shortcomings of atomic models

To-DO: Shortcomings of PT-based reduced-models

- Assumes a rigid substrate with a simplified potential shape.
- Energy dissipation is added through a viscous term $-m\mu\dot{x}$ being the only dissipation channel available. Does not capture a more complex real-life electron and phonon dissipation. Taking phonon dissipation as an example there are many vibration modes ($3N$). This will affect the thermal activation derivation.
- The moving body is simplified as a constantly moving rigid body, while in fact this will also be subject to a more complex dynamic behavior.

2.4.5 Experimental procedures

Experimentally, the study of nanoscale friction is challenging due to the low forces on the scale of nano-newtons along with the difficulties of mapping the nano-scale topography of the sample. In contrast to numerical simulations, which provide full transparency regarding atomic-scale structures, sampling of forces, velocities and temperature, the experimental results are limited by the state-of-the-art experimental methods. To compare numerical and experimental results we address a few of the most relevant experimental methods.

2.4.5.1 Scanning Probe Microscopy

Scanning probe microscopy (SPM) includes a variety of experimental methods which is used to examine surfaces with atomic resolution [61, pp. 6-27]. This was originally developed for surface topography imaging, but today it plays a crucial role in nanoscale science as it is used for probe-sampling regarding tribological, electronic, magnetic, biological and chemical character. The family of methods involving the measurement of forces is generally referred to as *scanning force microscopies* (SFM) or for friction purposes *friction force microscopes* (FFM).

One such method arose from the *atomic force microscope* AFM, which consists of a sharp micro-fabricated tip attached to a cantilever force sensor, usually with a sensitivity below 1 nN all the way down to pN. The force is measured by recording the bending of the cantilever, either as a change in electrical conduction or more commonly, by a light beam reflected from the back of the cantilever into a photodetector [1, p. 183]. By adjusting the tip-sample height to keep a constant normal force while scanning across the surface, the AFM can be used to produce a surface topography map. By tapping the material (dynamic force microscopy) with

a sinusoidally vibrated tip the effects from friction and other disturbing forces can be minimized to produce an even clearer image (include example, preferably showing the surface structure of graphene). However, when scanning perpendicularly to the cantilever axis, one is also able to measure the frictional force as torsion of the cantilever. By having four quadrants in the photodetector (as shown in figure Fig. 2.13), one can simultaneously measure the normal force and friction force as the probes scan across the surface.

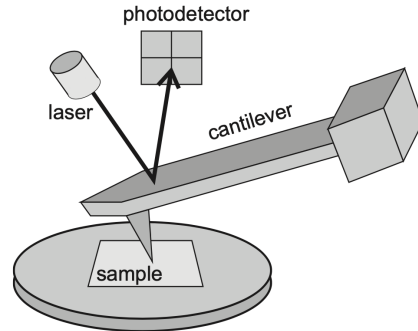


Figure 17.1 Schematic diagram of a beam-deflection atomic force microscope.

Figure 2.13: [Temporary] figure from [1, p. 184]

AFM can also be used to drag a nanoflake across the substrate as done by Dienwiebel et al. [57], where a graphene flake was attached to a FFM tip and dragged across graphite. Notice that this makes the normal loading concentrated to a single point on the flake rather than achieving an evenly distributed load.

2.4.5.2 Surface Force Apparatus

The Surface force apparatus SFA is based on two curved molecularly smooth surfaces brought into contact [1, p. 188]. The sample is placed in between the two surfaces as a lubricant film for which the friction properties can be studied by applying a tangential force to the surfaces.

2.5 Summary of previous results

Several studies have investigated the frictional behavior of graphene by varying different parameters such as normal force, sliding velocity, temperature, commensurability and graphene thickness [62]. In general, we find three types of relevant systems being studied: 1) An FFM type setup where the graphene, either resting on a substrate or suspended, is probed by an AFM tip scanning across the surface. 2) A SFA setup with the graphene “sandwiched” in between two substrate layers moving relative to each other using the graphene as a solid lubricant. 3) A graphene flake sliding on a substrate, either being dragged by an AFM tip or by more complex arrangements in numerical simulations. Considering that even the sharpest AFM tip will effectively put multiple atoms in contact with the sample, all methods are relatable to the study of nanoscale surface contacts. However, the FFM type is more reminiscent of asperity theory as we expect it to deform with increasing load, while the latter two are more aligned with the PT type models and our specific system of interest. Nonetheless, we will consider results across all three types of systems with the relevant studies summarized in Table 2.1 for convenience.

Table 2.1: Update multirow line span after completing the table...

System	Type	Year	Researcher	Materials	Keywords
FFM	Exp.	2007 [63]	Zhao et al.	Si ₃ N ₄ tip on graphite.	Temperature dependence
		2015 [64]	G. Paolicelli et al.	Si tip, graphene on SiO ₂ and Ni(111) substrate	Layers, load, shear strength
	Both	2019 [65]	Zhang et al.	Monolayer graphene	Straining sheet
		2019 [66]	Vazirisereshk et al.	Graphene, MoS ₂ and Graphene/MoS ₂ heterostructure	Low friction?
	Num.	2015 [67]	Yoon et al.	Si tip, graphene on SiO ₂	Stick-slip: tip size, scan angle, layer thickness, substrate flexibility
		2016 [68]	Li et al.	Si tip, graphene on a-Si substrate	Increasing layers
	SFA	2011 [69]	Wijn et al.	Graphene flakes between graphite	Rotational dynamics, superlubricity, temperature
		2012 [30]	H. J. Kim and D. E. Kim.	Carbon sheet	Corrugated nano-structured surfaces
Flake	Exp.	2005 [57]	Dienwiebel et al.	Graphene on graphite	Commensurability, superlubricity
		2013 [70]	Feng et al.	Graphene on graphite	Free sliding
	Num.	2009 [71]	Bonelli et al.	Graphene on graphite	Tight-binding, commensurability, load, flake size
		2012 [72]	Reguzzoni et al.	Graphene on graphite	Graphite thickness
		2014 [73]	Liu et al.	Graphene on graphite	Thickness, deformations, high speed
		2018 [74]	P. Zhu and Li	Graphene on gold	Flake size, commensurability
		2019 [75]	Zhang et al.	Graphene on diamond	Temperature, sliding angle, friction coefficient

One of the earliest tribological simulations of graphene was carried out by Bonelli et al. [71] in 2009 using a tight-binding method (excluding thermal excitations) to simulate a graphene flake on an infinite graphene sheet [62]. They implemented a FKT-like setup where each atom in the flake is coupled horizontally to a rigid support by elastic springs. They recovered the stick-slip behavior, which is also observed in FFM setups both experimentally [63, 65] and numerically [68, 74]. Moreover, they found an agreement with the qualitative observation that soft springs allow for a clean stick-slip motion while hard springs ($\sim 40 \text{ N/m}$) inhibited it, which also aligns with the PT model. In AFM and SFA experiments, the stick-slip motion tends to transition into smooth sliding when the speed exceeds $\sim 1 \mu\text{s}$ while in MD modeling the same transition is observed in the $\sim 1 \text{ m/s}$ region [17]. More precisely Liu et al. [73] findes the transistion MD simulations at 15 m/S. This 6-order-of-magnitude discrepancy has been largely discussed in connection to simplifying assumptions in MD simulations. On the other hand, the PT model qualitatively disagrees as it predicts smooth sliding for low speeds and stick-slip for high speeds. However, in an extension of the PT for the study of nanoscale rolling friction by Sircar and Patra [76], they found smooth sliding for high speeds.

Bonelli et al. [71] also found that commensurability, through orientation of the flake and the direction of sliding, had a great impact on the frictional behavior which generally aligns with the predictions of the FK and FKT models. They confirmed qualitatively the observation of superlubricity for certain incommensurable orientations which has been reported in experiments by Dienwiebel et al.[57] and further supported by experimental measurements of interaction energies by Feng et al. [70]. The importance of commensurability is also reported for MD simulations [69, 74, 75]. Bonelli et al. found the friction force and coefficient to be one order of magnitude higher than that of the experimental results which they attribute to the details of the numerical modeling. Generally, the experimental coefficients between graphite and most materials lie in the range of 0.08–0.18 [57].

While Dienwiebel et al. [57] reported a wide range of frictional forces from 28 ± 16 pN to 453 ± 16 pN with loads $\sim [-10, 20]nN$, the change in friction with applied load was as low as 0.05–0.4 % for the incommensurable orientations. When using the slope definition for the frictional coefficient Eq. (2.2b), this corresponds to a coefficient in the range of 0.0005–0.004. Bonelli et al. attribute the low dependency to a lacking change in contact area as the flake is loaded.

Furthermore, Bonelli et al. [71] found friction to decrease with increasing flake size which is also reported in MD simulations for graphene on gold [74]. Bonelli et al. mainly attribute this to boundary effects, but also note that the coupling to the support made for decreased rotational freedom as flake size was increased. Thus, they hypothesized that the decreased freedom led to the graphene taking a more forced path which is associated with a decreased stick-slip behavior. The general observation however, disagrees with the FK and FKT model which predicts the reverse; an increase in friction with increasing size.

An additional numerical study of monolayer islands of krypton on copper by Reguzzoni and Righi [77], supports the importance of commensurability regarding size effects, as they report that the effective commensurability increase drastically below a critical flake radius on the order of 10 Å. In a numerical study by Varini et al. [78], based on Kr islands adsorbed on Pb(111), this is further elaborated as they found that finite size effects are especially important for static friction due to a pinning barrier arising from the edge, preventing otherwise superlubricity due to incommensurability. They reported a relationship $F_s \sim A^{\gamma_s}$ not only sublinear, $\gamma_s < 1$, but also sublinear with respect to the island perimeter, $P \propto A^{1/2}$, by having $\gamma_s = 0.25$ for a hexagonal edge and $\gamma_s = 0.37$ when circular, indicating that only a subset of the edge is responsible for the pinning effect. This aligns with the general change in friction found by [74] for different flake geometries (square, triangle, circle). Additionally, Varini et al. found the edge pinning effect to decrease with increasing temperature as the edge energy barriers are reduced. Bringing all this together, the main picture forming is that flake size, which can be related to contact area, is affecting friction through a commensurability mechanism. If the flake is constrained in some way we might not observe the same dependency. While flake size nor contact area is easily measured in experimental FFM, Mo et al. [27] found in an MD simulation that friction is proportional to contact area for an indenting sphere on a nanoscale.

Evolution effects, or so-called friction strengthening, are also observed. That is, friction increases during the initial stick-slip cycles, which is observed experimentally by Zhang et al. [65] and numerically by Li et al. [68]. However, this is only found when having the graphene sheet resting on a substrate [65], as opposed to a suspended sheet. It is also found to diminish with an increasing number of graphene layers stacked (graphite) [68]. In the study by Li et al., they reported a general decrease in friction with an increasing number of layers which is found in other MD studies [67] and experimental studies as well [79, 80]. However, we also found an MD study reporting the opposite trend [72].

A few numerical studies investigate friction under mechanical deformations. Zhang et al. [65] found that straining a suspended graphene sheet will lower the kinetic friction. They attribute this to modulation of flexibility which consequently changes the local pinning capability of the contact interface. Liu et al. [73] carried out an MD simulation of high-speed (400 m/s) ballistic nanofriction of graphene on graphite. They found that a biaxial stretching of the graphitic substrate could be used to suppress frictional scattering and achieve persistent superlubricity. Another surface manipulating study was performed by H. J. Kim and D. E. Kim [30] who investigated the effects of corrugated nano-structured surfaces. The study revealed that corrugated surfaces with altered contact areas and structural stiffness could result in both increased or slightly decreased friction under certain load ranges. Altogether these studies highlight the importance of surface structure and mechanical conditions.

The friction dependency of normal load turns out to be a complex matter and has proven to be a highly system-dependent feature. As already mentioned, asperity theory mainly points to a sublinear relationship between friction and load, while the reduced-models point to a more intricate relationship through the change of the effective substrate potential which leads to an altering of the commensurability and the phonon dynamics. Experimentally rather different trends have been observed, although the majority agree on increasing friction with increasing load [1, p. 200]. For the graphene flake, Dienwiebel et al. [57] found a seemingly non-dependent relationship while FFM study by G. Paolicelli et al. [64] found a sublinear relationship matching the predictions of Maugis-Dugdale theory ($F_f \propto (F_N - F_{N,0})^{2/3}$). The discrepancy might be attributed to the difference in system type; A spherical tip indenting the graphene sheet as opposed to the atomic flatness of the graphene-graphite interface, which does not make for a changing contact area under load. However, numerical studies using a graphene-graphite interface still find both sublinear [71] and linear [65, 75] load dependencies.

In an experimental FFM study by Deng et al. it was discovered that the friction force kept increasing after unloading the probe tip from the graphite surface. This has been argued to be a more general phenomenon related to hysteresis in the adhesive interaction between two sliding bodies [81]. Following the slope definition for the friction coefficient, these results correspond to a negative friction coefficient. More recently, a negative friction coefficient has also been observed for the loading phase by Liu et al. [14] in an experimental study of the interface between graphite and muscovite mica heterojunction. With supporting numerical modeling this is attributed to “synergetic and nontrivial redistribution of water molecules at the interface”. Similar results are also reported numerically by [15] for graphite in contact with hexagonal boron nitride heterojunctions which is attributed to “load-induced suppression of the moiré superstructure out-of-plane distortions leading to a less dissipative interfacial dynamics”. Thus, the concept of a negative friction coefficient has been proven for the unloading phase of adhesive contacts and in the loading phase for a few systems.

The dependency of velocity is generally found to increase logarithmically with velocity in experimental AFM studies [1, p. 201] which match the low-velocity regime of the PT type models. At higher velocities, thermally activated processes are less important and friction becomes independent of velocity according to the PT model result Eq. (2.6) when ignoring the athermal regime. Saturation of the velocity dependency has been observed numerically for Si tips interacting with diamond, graphite and amorphous carbon surfaces respectively with scan velocities above $1 \mu\text{m/s}$ [82]. Guerra et al. [83], studying gold clusters on graphite using MD simulations, found a viscous friction response, friction being proportional to sliding velocity, in both low and high speed domains. However, thermal effects reversed as they found friction to decrease with increasing temperature at low speed (diffusive regime), but for high speed (ballistic regime) they found an increasing friction with temperature. In the MD simulations this crossover from ballistic to diffusive occurred between 10 and 1 m/s .

Regarding temperature itself, the general experimental trend is decreasing friction with increasing temperature as found by Zhao et al. [63] in a series of AFM graphene on graphite experiments yielding $F_{\text{fric}} \propto \exp(1/T)$. This agrees with the thermal drift regime of the PT model even though the exact temperature range does not agree. Moreover, Wijn et al. [69] found that friction commensurability can be lost at higher temperatures (above 200K) where they found a power law behavior $F_k \propto T^{-1.13 \pm 0.04}$. Numerically, Zhang et al. [75] found that friction increased with temperature, using a sliding speed of 10 m/s . Considering the findings of [83] this qualitative different behavior might be attributed to an MD related effect associated with the transition from low speed diffusive behavior as to high speed ballistic behavior.

From the review of previous results, we find several gaps and discrepancies in the description of friction provided by the reduced-models, MD simulations and experimental methods respectively. Some of the discrepancies can be attributed to the fact that different physical mechanisms are included in the numerical modeling. The reduced-models provides the simplest description while MD simulations are thought to capture a more complex behavior. On the other hand, we might also point differences in the studied systems as an important factor to consider. This regard the physical conditions such as sliding speed and temperature, but also higher level features concerning the mechanical properties of the system. For instance, the FFM based results consider an asperity-like system where the tip is expected to deform under loading, which gives rise to a change in contact area. This feature is lacking in the flat flake-/sheet-systems, and thus we might question the role of the contact area in these systems. More precisely, when inflicting an out-of-plane buckling through Kirigami cuts and stretching, the contact area is expected to decrease as well. From asperity theory we might simply hypothesize that friction will decrease during such a transition. However, as the system deforms we can also expect a modification of the commensurability, and the local loading which can be associated with radical changes in the frictional behavior associated with different stick-slip regimes. From the results of a non-Kirigami sheet under tension, we already see clues that the stretching will provide a reduction in friction without considering the contact area. Similar, the results from a corrugated nano surface also points to the fact that surface stiffness might play an important role as well.

2.6 Research questions

Based on the review of friction presented in Chapter 2, it is evident that the behavior of friction is significantly influenced by various factors, such as the specific system under investigation, the numerical modeling approach, and the physical conditions related to the environment and the probing of friction. In our study, we aim to investigate the frictional behavior of a Kirigami sheet under the effects of strain. Previous studies have demonstrated that strained Kirigami sheets are prone to exhibiting out-of-plane buckling [6, 7] which is indicative

of a possible transition between two distinct systems: an atomically flat interface and an asperity system. These systems are usually only studied separately, and thus our primary objective is to explore the potential frictional effects associated with system transitions resulting from the straining of a Kirigami sheet. In particular, we want to investigate the significance of the contact area and evaluate the hypothesis that reducing the contact area will lead to a decrease in friction. Additionally, we seek to examine the relationship between the friction-load curve and this phenomenon. For the sake of contributing new insight to the field of nanoscale friction, we are especially interested in non-linear dependencies between friction and stretching of various Kirigami designs. Drawing on this perspective, we aim to investigate the prospects of achieving a negative friction coefficient for a system of coupled load and stretch. The relevant understanding of how physical conditions affect frictional behavior in experimental and numerical studies will be considered in order to frame our results within the theoretical understanding.

To gain a more comprehensive understanding of the potential applications of Kirigami design, we aim to develop a dataset based on MD simulations that capture the frictional effects on Kirigami designs when subjected to stretching and loading. We intend to employ machine learning techniques to discern any meaningful trends in the data that may be used to inform future research endeavors. Specifically, we seek to leverage the machine learning model to facilitate an accelerated search for optimizing specific frictional properties. Our focus will be on evaluating the prospects of reducing or increasing the friction force, as well as reducing or increasing the friction coefficient for a coupled system of load and stretch. Our main research questions can be summarized as follows.

1. How can we design an MD simulation that provides a reliable foundation for an investigation of the friction behavior for a Kirigami graphene sheet sliding on a substrate? How do physical conditions such as temperature and sliding speed control the frictional behavior?
2. How can we design an ensemble of Kirigami patterns for the investigation of its frictional properties with the scope of getting out-of-plane buckling and also randomized design features?
3. Can we control friction for a Kirigami sheet through pattern design and stretching of the sheet?
 - (a) How does friction dependent on a changing contact area?
 - (b) How does the friction-load curve relate to stretched Kirigami sheets?
 - (c) Are the effects of stretching and pattern design significant when considered independently?
4. Is it possible to utilize machine learning techniques to identify general trends in friction associated with Kirigami designs, stretch and load?
5. Can we use a trained machine learning model to predict new designs through accelerated search?
6. What are the prospects of achieving a negative friction coefficient for a system of coupled load and stretch through Kirigami design?

Part II

Simulations

Chapter 3

Pilot study

Having defined our system, we carry out an initial study of the frictional properties. First, we evaluate the numerical results for a non-cut sheet in order to define suitable metrics for a numerical evaluation of friction and justify some of the default parameter choices. This provides a basis for the following study where we consider the Tetrahedron and Honeycomb Kirigami patterns as well. We conduct a more systematic investigation of the friction dependencies to temperature, sliding speed, spring constant and timestep. Finally, we consider the mean friction of all three configurations when stretched. This includes an analysis of the dependence to contact area and the friction-load curves.

3.1 Friction simulation parameters

The MD simulations we will carry out to measure friction are governed by a small set of parameters. For the purpose of creating a machine learning we need to standardize these parameters. This we keep most of them constant with only a small subset of parameters being varied: sheet configuration, strain and load. Instead of starting with the parameter selection process, we first state the final choice in Table 3.1. Due to the great number of parameters, we do not make an exhaustive search of all parameters before deciding on the final settings. Instead, we take a basis in parameters used in similar friction simulations [67, 68, 73–75] and adjust accordingly to the aim of getting stable measurements and reducing computation time where possible. Parameters such as initial relaxation time, pauses and strain speed are chosen mainly from the results of initial stability tests. The sheet and pull block sizes are chosen with a consideration of the balance between Kirigami design options and computational resources. The scan direction is chosen to be parallel to the connection line between the pull blocks. This is mainly chosen in order to avoid unecessary complexity in the motion since it can be hypothesized that the center of the sheet can drag behind for other scan directions. The remaining parameters: Temperature T , sliding speed v_{slide} , spring constant K , normal load F_N , timestep dt and sliding distance have been chosen because the friction output remains relatively stable with moderate perturbations around these default values. We will explain this in more detail later in the chapter. Note that the default values in Table 3.1 will be used when nothing else is stated explicitly.

Table 3.1: Parameters involved for the numerical MD simulation for measuring friction. The default values correspond to the final choice used for the dataset. The shaded cells denote the parameters varied in the ML dataset.

Parameter	Default value	Description
T	300 K	Temperature of the system.
v_{slide}	20 m/s	Sliding speed for the sheet translation.
K	∞	Spring constant for the coupling between the virtual atom and the sheet pull blocks.
Scan direction	$(x, y) = (0, 1)$ (zigzag direction)	The direction for which we translate the sheet.
Sheet configuration	Contiguous	Binary mapping describing which atoms are removed (0) and which is still present (1) in the graphene sheet.
Strain amount	[0, rupture]	The ratio of change in length to the original length.
F_N	[0.1, 10] nN	Applied normal force to the pull blocks.
dt	1 fs	MD integration timestep.
Initial relaxation time	15 ps	Initial relaxation time before straining.
Pauses	5 ps	Relaxation pauses after strain, and during the normal load phase (before translating the sheet).
Strain Speed	0.01 ps^{-1}	The rate of straining for the sheet.
Slide distance	400 Å	How far the sheet is translated.
Sheet size	$130.029 \times 163.219 \text{ \AA}$	Spatial 2D size of the sheet.
Pull block size	$2 \times 130.029 \times 15.183 \text{ \AA}$	Spatial 2D size of the pull blocks.

3.2 Force traces

We begin by assessing the friction force traces, i.e. force vs. time curves, for a single friction simulation using the default parameters shown in Table 3.1 for a non-cut sheet with no stretch applied and a normal load of 1 nN.

3.2.1 Force oscillations

We evaluate the friction force as the force acting on the sheet from the substrate. We consider initially the force component F_{\parallel} parallel to the drag direction as plotted in Fig. 3.1. We use a sample rate of $10 \text{ ps}^{-1} = 100 \text{ timesteps}^{-1}$ for which each sample is the mean value of the preceding 100 timesteps. We observe immediately that the data carries oscillations on different time scales which match our general expectations for sliding involving periodic surfaces. By applying a Savgol filter to the data with a polynomial order of 5 and a window length of 150 timesteps (corresponding to a sliding distance of 3 Å or a time window of 15 ps) we can qualitatively point out at least two different frequencies of oscillation. During the first 10 Å of sliding, seen in Fig. 3.1a, we see roughly three waves on the Savgol filter corresponding to a relatively high frequency, while for the duration of 100 Å of sliding, seen in Fig. 3.1b, the same Savgol filter reveals a lower frequency on top, creating the visual pattern of a wavepacket. The data does not indicate clear signs of stick-slip behavior as otherwise found in other studies, e.g. by Zhu and Li [74] for graphene on gold, who saw a more typical saw tooth shape in the force trace. Besides the difference in the substrate material, using gold instead of silicon, they used a lower sliding speed of 10 m/s and a soft spring of $K = 10 \text{ N/m}$. By adopting these parameters we get a slightly different force trace behavior as shown in Fig. 3.1c and Fig. 3.1d. This change breaks the symmetry in the force oscillations but still does not produce any significant discontinuities in the trace. By keeping the spring constant $K = 10 \text{ N/m}$ and lowering the sliding speed further down to 1 m/s we are able to demonstrate a proper stick-slip behavior as shown in Fig. 3.1e and Fig. 3.1f. Considering all three simulations we might classify the results from the default settings, $K = \text{inf}$, $v = 20 \text{ m/s}$, as smooth sliding, $K = 10 \text{ N/m}$, $v = 10 \text{ m/s}$, as a transition phase with possible occasional slipping, and $K = 10 \text{ N/m}$, $v = 1 \text{ m/s}$ as certain stick-slip behaviour.

This confirms the qualitative observation the stick-slip behavior is suppressed with stiff springs [71] springs and high sliding velocity [73]. Having a low sliding speed comes with a high computational cost which is the reason that we choose a relatively high sliding speed of 20 m/s. The choice of an infinite spring constant is related to the stability of the measurements and is discussed later in this chapter make sure it is, maybe make a reference.

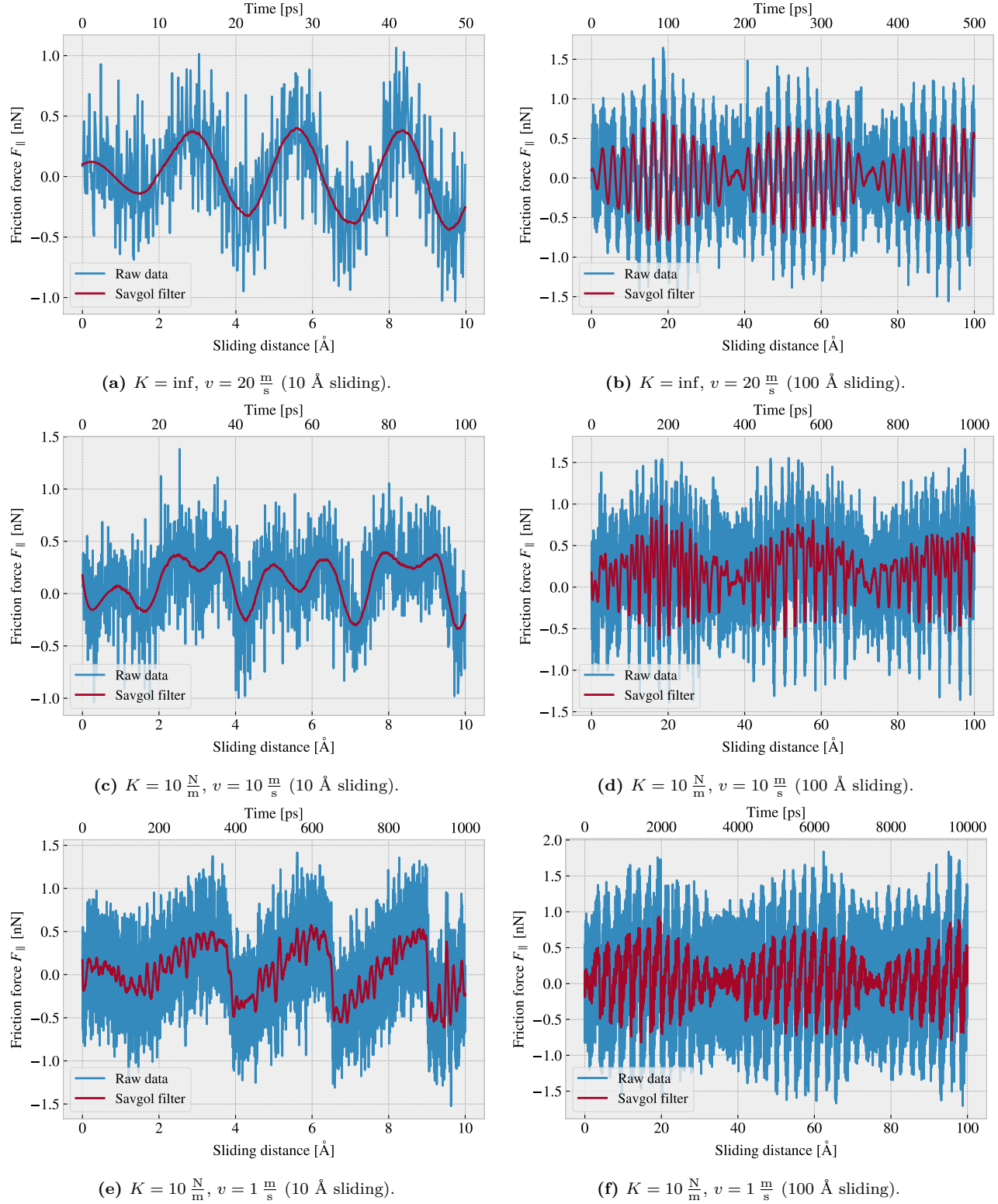


Figure 3.1: Force traces of the friction force F_{\parallel} with respect to the drag direction acting from the substrate on the full sheet. The force traces are plotted against the sliding distance (lower x-axis) and the corresponding sliding time (upper x-axis). The sliding distance is measured by the displacement of the virtual atom tethering the sheet. The red line represents a Savgol filter with polynomial order 5 and a window length of 150 timesteps (corresponding to a sliding distance of 3 \AA or a time window of 15 ps). Each row, (a,b), (c,d), (e,f), represents a different choice of the spring constant K and sliding speed v , while the columns show the same result for two different time scales. The default settings are represented in figure (a) and (b).

By performing a Fourier Transform on the data, using the default parameters, we can quantify the leading frequencies observed in figure Fig. 3.1a and Fig. 3.1b. The Fourier transform is shown in Fig. 3.2a, and by plotting the two most dominant frequencies $f_1 = 0.0074 \text{ ps}^{-1}$ and $f_2 = 0.0079 \text{ ps}^{-1}$ as a sine sum, $\sin(2\pi f_1) + \sin(2\pi f_2)$, we find a qualitatively convincing fit to the observed wavepacket shape as seen in Fig. 3.2b. We can convert the frequencies according to that of a wavepacket. By using the trigonometric identity

$$\begin{aligned}\sin(a+b) &= \sin(a)\cos(b) + \cos(a)\sin(b), \\ \sin(a-b) &= \sin(a)\cos(b) - \cos(a)\sin(b),\end{aligned}$$

and decomposing the frequencies as $f_1 = a - b$, $f_2 = a + b$, we can rewrite the sine sum as the sinusoidal product

$$\begin{aligned}\sin(2\pi f_1) + \sin(2\pi f_2) &= \sin(2\pi(a-b)) + \sin(2\pi(a+b)) \\ &= \sin(2\pi a)\cos(2\pi b) + \cancel{\cos(2\pi a)\sin(2\pi b)} + \sin(2\pi a)\cos(2\pi b) - \cancel{\cos(2\pi a)\sin(2\pi b)} \\ &= 2\sin(2\pi a)\cos(2\pi b),\end{aligned}$$

with

$$\begin{aligned}a &= \frac{f_1 + f_2}{2} = 0.0763 \pm 0.0005 \text{ ps}^{-1}, & b &= \frac{f_2 - f_1}{2} = 0.0028 \pm 0.0005 \text{ ps}^{-1}, \\ &= 0.381 \pm 0.003 \text{ \AA}^{-1}, & &= 0.014 \pm 0.003 \text{ \AA}^{-1}.\end{aligned}$$

In the latter transition, we have denoted the frequency with respect to the sliding distance by considering the default sliding speed of 20 m/s = 0.2 Å/ps. This makes us recognize the high oscillation frequency as a and the low frequency as b . The faster one has a period of $T_a = 2.62 \pm 0.02 \text{ \AA}$ ² which corresponds well with the magnitude of the lattice spacing and especially that of graphene at 2.46 Å as expected theoretically. The longer period $T_b = 71 \pm 15 \text{ \AA}$ is not obviously explained. We notice a similarly long period oscillation for all three cases Fig. 3.1b, Fig. 3.1d and Fig. 3.1f, and thus we have no reason to believe that this is dependent on the stick-slip behavior. The initial build-up in friction force is reminiscent of friction strengthening, which is often reported [65, 68], but the periodicity goes against this idea. Instead, we might attribute it to some phonon resonance which could be a physical phenomenon or simply a feature of our MD modeling.

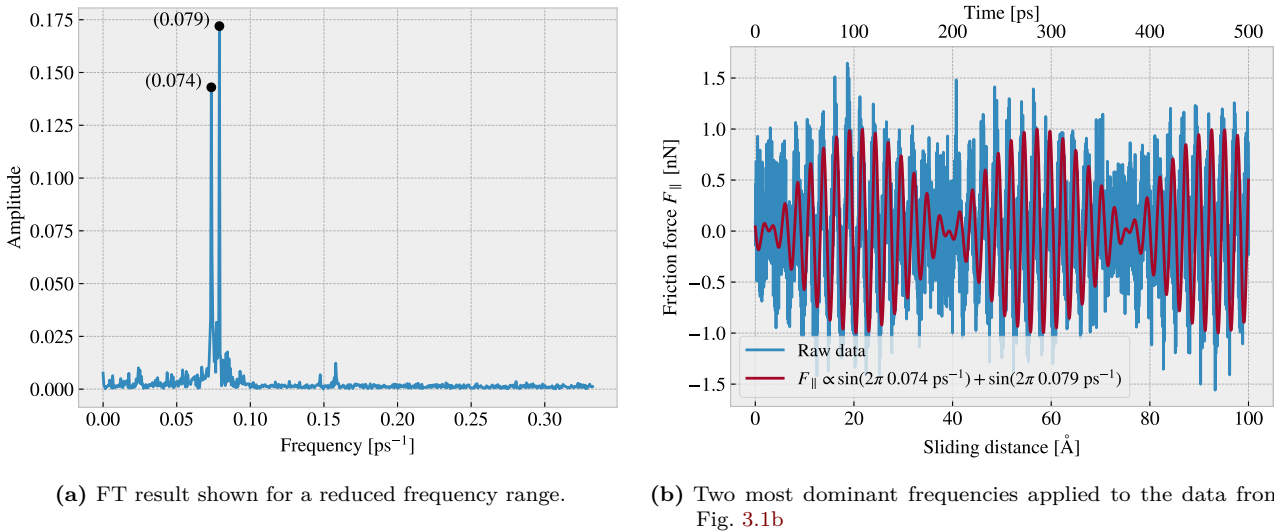


Figure 3.2: Fourier transform analysis of the full friction force data (all 400 Å sliding distance) shown in Fig. 3.1. (a) shows the two most dominant frequency peaks. Note that no significant peaks were found in a higher frequency than included here. (b) shows a comparison between the raw data and the wavefunction corresponding to the two peaks in figure (a).

²The uncertainty Δy is calculated as $\Delta y = \left| \frac{\partial y}{\partial x} \Delta x \right|$ for uncertainty Δx and $y(x)$

3.2.2 Decompositions

In the previous analysis, we looked only at the friction force for the full sheet, including the rigid pull blocks, and with respect to the drag direction. We found this way of measuring the friction force to be the most intuitive and reliable, but we will present the underlying arguments for this choice in the following.

Since we are only applying cuts to the inner sheet, and not the pull blocks, it might appear more natural to only consider the friction inner sheet. If the desired frictional properties can be achieved by altering the inner sheet one can argue that any opposing effects from the pull blocks can be mitigated by simply scaling the relative size between the inner sheet and the pull blocks. However, when looking at the force traces decomposed with respect to the inner sheet and pull block regions respectively in Fig. 3.3a, we observe that the friction force arising from those parts is seemingly antisymmetric. That is, the distribution of the frictional pull from the substrate on the sheet is oscillating between the inner sheet and the pull blocks. Keeping in mind that normal force is only applied to the pull blocks we might take this as an intrinsic feature of the system that does not necessarily disappear with a scaling of the spatial ratio between the inner sheet and pull blocks. Any interesting friction properties might depend on this internal distribution of forces. Hence, we hedge our bets and use the full sheet friction force as a holistic approach to avoid excluding relevant information in the measurement data.

Similarly, we might question the decision of only considering the frictional force projected onto the sliding direction as we are then neglecting the “side shift” induced during sliding. In Fig. 3.3b we show the decomposition in terms of the force components parallel F_{\parallel} and perpendicular F_{\perp} to the sliding direction respectively. We notice that the most dominant trend appears for the parallel component. If we want to include the perpendicular component as well we would have to evaluate friction as the length of the force vector instead. However, this would remove the sign of the force direction and shift the mean friction force up as we see both negative and positive contributions in the parallel force trace. One option to accommodate this issue is by using the vector length for the magnitude but keeping the sign from the parallel component. However, we omit such compromises as this might make the measurement interpretation unnecessary complex, and we use only the parallel component going forward.

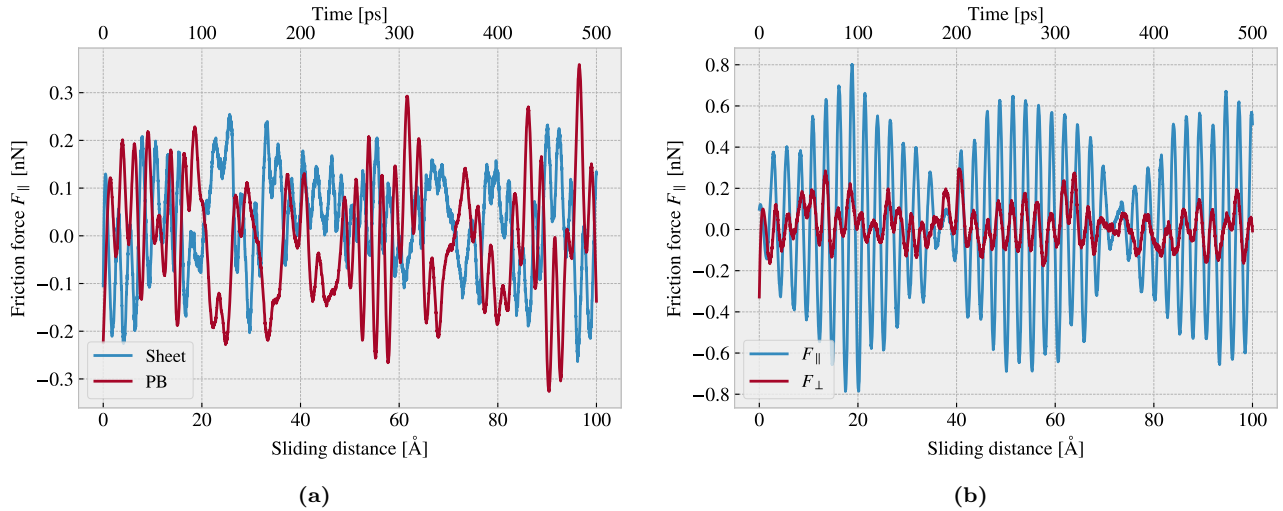


Figure 3.3: Friction force decomposition on the default parameter force trace shown in Fig. 3.1 showing only the applied Savgol filters. (a) Decomposition into group inner sheet (sheet) and pull blocks (PB). (b) Decomposition into parallel (F_{\parallel}) and perpendicular (F_{\perp}) to drag sliding direction.

3.2.3 Center of mass path

From the previous observations of the force traces in Fig. 3.1 we found both smooth sliding and stick-slip behavior depending on the sliding speed and spring constant. Considering the force decomposition in Fig. 3.3b we know that a frictional force in the perpendicular direction to sliding is also present. By looking at the x, y -position for the sheet Center of Mass (CM) we find a qualitatively different behavior when reconsidering the spring constants and sliding speeds investigated in Fig. 3.1. These results are shown in Fig. 3.4. The default case in Fig. 3.4a shows a rather straight path forward with only a small side motion in comparison to the cases

in Fig. 3.4b and Fig. 3.4c. However, the CM accelerates and deaccelerates with a high frequency, much too high to be associated with the lattice spacing on the order of 2.46 \AA . One possible explanation is that the sheet and substrate constitute an incommensurable contact for which traveling kink excitations make the atoms move in such a way that the sheet CM is incremented in small ‘‘burst’’. When looking at the $K = 10 \frac{\text{N}}{\text{m}}$, $v = 10 \frac{\text{m}}{\text{s}}$ case in Fig. 3.4b we see a completely different CM path where the rapid movements aligns visually better with the force oscillations shown earlier in Fig. 3.1d. The CM accelerates forward and then deaccelerates in combination with a side motion that leads to the CM path making a loop as it slows down. Finally we have the $K = 10 \frac{\text{N}}{\text{m}}$, $v = 1 \frac{\text{m}}{\text{s}}$ in Fig. 3.4b which is confirmed to have stick-slip behavior in Fig. 3.1f. Here the CM path shows a more chaotic movement between acceleration, but with the rapid parts aligning which also visually well with the timing of the slips seen in Fig. 3.1f. The chaotic motion is not connected to the stick-slip motion, but we might associate it with the thermal contributions being dominant in this regime.

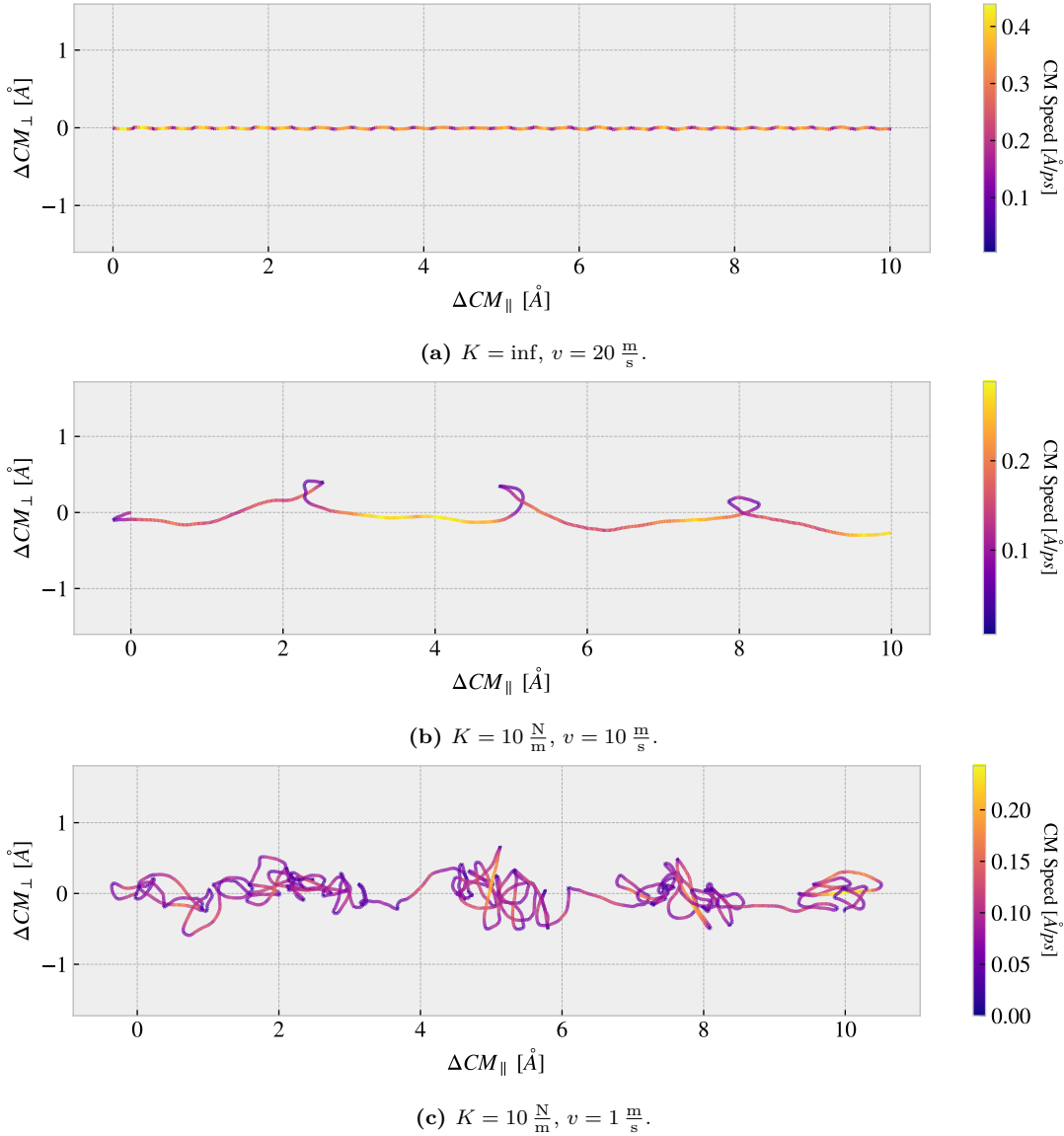


Figure 3.4: Center of Mass (CM) position relative to the start of the sliding phase in terms of the direction parallel to the sliding direction ΔCOM_{\parallel} and the axis perpendicular to the sliding direction ΔCOM_{\perp} . The colorbar denotes the absolute speed of the CM motion. Figure a-c shows different parameters used for the spring constant K and sliding speed v similar to that used in Fig. 3.1. (a) Default: $K = \infty$, $v = 20 \frac{\text{m}}{\text{s}}$. (b) $K = 10 \frac{\text{N}}{\text{m}}$, $v = 10 \frac{\text{m}}{\text{s}}$. (c) $K = 10 \frac{\text{N}}{\text{m}}$, $v = 1 \frac{\text{m}}{\text{s}}$

3.3 Defining metrics for friction

In order to evaluate the frictional properties of the sheet we aim to reduce the force trace results, addressed in section Sec. 3.2, into single metrics describing the kinetic and static friction respectively.

3.3.1 Kinetic friction

We measure kinetic friction as the mean of the friction force trace. More precisely, we take the mean value of the last half of the dataset in order to ensure that we are sampling from a stable system. For a full sliding simulation of 400 Å our mean value will be founded on the last 200 Å (1000 ps) of sliding. In Fig. 3.5a we have shown the force trace for the first 10 Å of sliding together with a 50% running mean window. The choice of such a short sliding distance is merely to illustrate the sampling procedure, and we see that the final mean estimate (marked with a dot) takes a negative value due to the specific cut-off of the few oscillations captured here. Nonetheless, one approach to quantify the uncertainty of the final mean estimate is to consider the variation of the running mean preceding the final mean value. The more the running mean fluctuates the more uncertainty associated with the final estimate. Only the running mean “close” to the ending should be considered, since the first part will rely on data from the beginning of the simulation. From the Fourier analyze in section Sec. 3.2.1 we found the longest significant oscillation period to be ~ 71 Å. Hence, we find it reasonable to use the standard deviation (std) for the last ~ 71 Å of the running mean window to evaluate the fluctuations. When including the full sliding length this corresponds to the last $\sim 35\%$ of the running mean window. We consider the std as an estimate of the absolute error and calculate the relative error by a division of the final mean value. In Fig. 3.5b we showcase a running relative error based on the std, with a window of length 35% the mean window, in a continuation of the illustrative case of a 10 Å sliding from Fig. 3.5a. In this case, we get an extremely high relative error of $\sim 257\%$, but this is consistent with the fact that the short sampling period leads to an unphysical negative value which should be associated with high uncertainty.

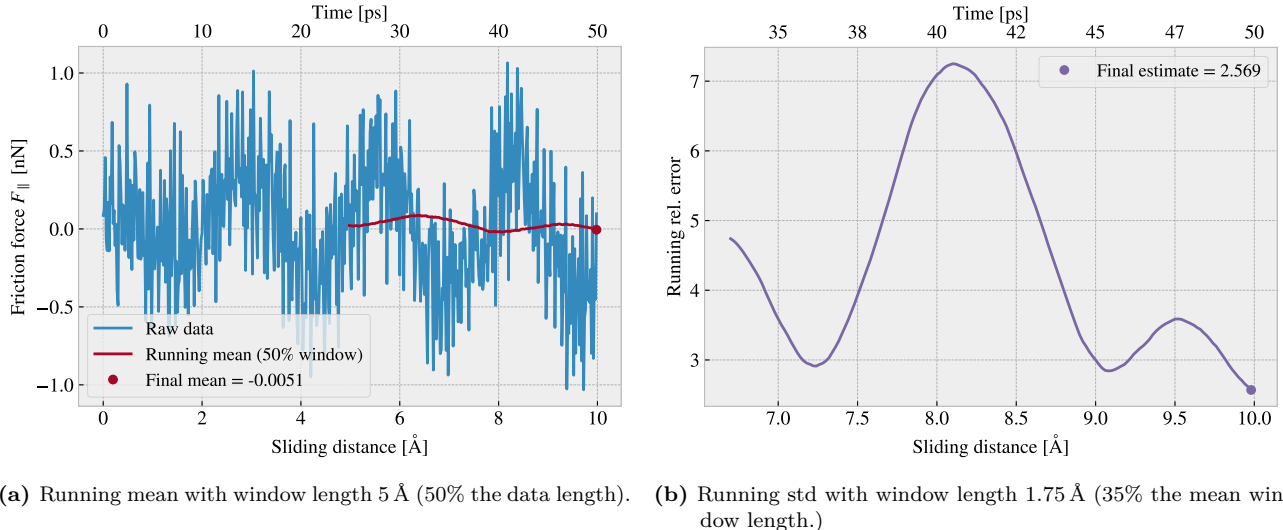


Figure 3.5: Running mean (a) and running relative error (std) (b) on the friction force data from a reduced sliding distance of 10 Å. The running mean window is 50% the data length while the running std window is 35% the running mean window length. The values are plotted at the end of their respective windows such that window precedes the actual point on the graph.

When including the full dataset of 400 Å of sliding, such that the std window actually matches with the longest period of oscillations expected, we get a final relative error of $\sim 12\%$ as shown in fig Fig. 3.6. This is arguable just at the limit of an acceptable error, but as we shall see later on in Sec. 3.6 this high relative error is mainly associated with the cases of low friction. When investigating different configurations under variation of load and strain we see a considerably lower relative error as the mean friction evaluates to higher values. One interpretation of this finding is simply that the oscillations in the running mean are to some degree independent of the magnitude of the friction. In that case, the relative error will spike for the low friction cases, and the

absolute error might be the more reliable measure, i.e. using simply the std without dividing by the final mean value.

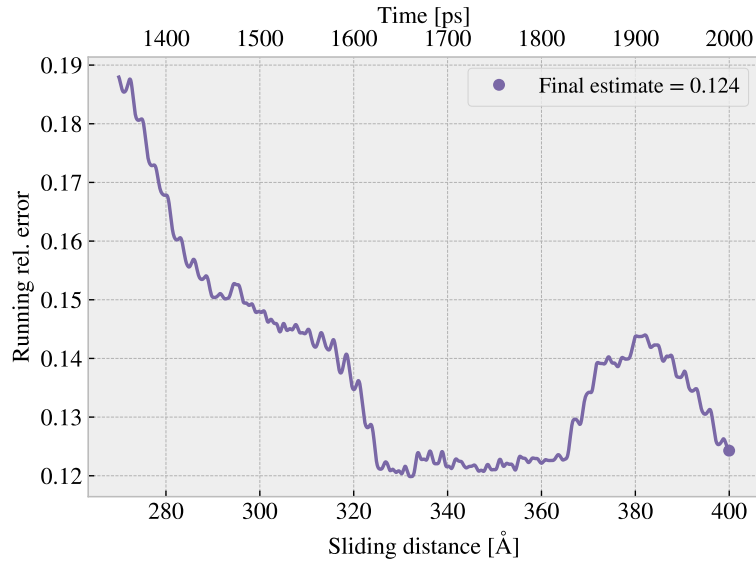


Figure 3.6: Running standard deviation (std) for a full 400 Å sliding simulation. The running std window is 70 Å (35% the running mean window of 50% the data length).

3.3.2 Static friction

The maximum value is one of the common choices for addressing static friction, even though the definition of static friction is a bit vague. When considering the force traces in Fig. 3.1 we observe that the force oscillations increase in magnitude toward a global peak at ~ 20 Å. Thus, one could be inclined to identify this peak as the maximum value associated with the static friction force. However, as we have already clarified, this steady increase in friction is part of a slower oscillation that repeats by a period of ~ 71 Å. By plotting the top three max values recorded during a full 400 Å simulation, for 30 logarithmically spaced load values in the range [0.1, 100] nN, we observe that the global max rarely falls within this first oscillation period as shown in Fig. 3.7. Only 2 out of 30 global maxima and 4 out of 90 top three maxima can be associated with the start of the sliding by this definition. Thus, this result suggests that our default system does not yield a static friction response in the sense of an initial increase in friction due to a depinning of the sheet from the static state. Some parameter changes that might increase the likelihood of seeing a significant static friction response are either extending the relaxation period since static friction is theorized to increase logarithmically with time [21], or increasing the sliding force more slowly through a soft spring tethering. As an attempt to test the latter part of this hypothesis we run a series of simulations with varying spring constant, $K \in [5, 200]$ nN including also $K = \infty$, but keeping the relaxation time and sliding speed at the default values. The result is shown in Fig. 3.8 and do not show any support for the hypothesis that a softening of the spring constant will eventually lead to the friction maximum occurring in the first period of sliding. We note that this might be suppressed by having a too short relaxation period or a too high sliding speed (related to the initial force increase), but due to the ambiguousness in the assessment of the static friction we will mainly concern ourselves with the kinetic friction in the remaining of this thesis.

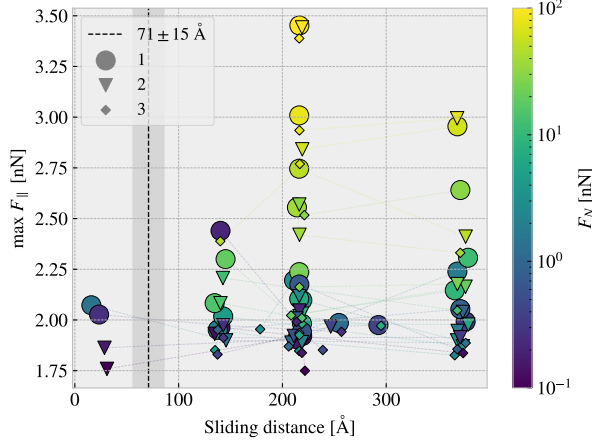


Figure 3.7: Distribution of top three max friction force peaks for 30 uniformly sampled normal forces $F_N \in [0.1, 10]$ nN. The dotted line and the grey area mark the slowest significant oscillation period found in the data and thus marking a dividing line for whether a peak falls within the “beginning” of the sliding simulation.

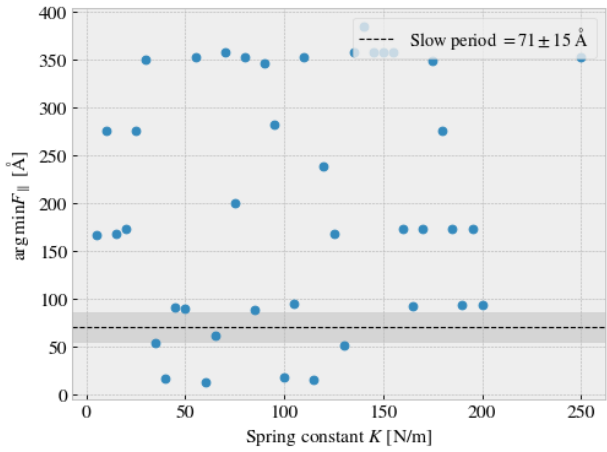


Figure 3.8: Sliding displacement for the max friction peak to appear as a function of spring constant. Fixmove is tmp mapped to $K = 200$ here without any discontinuous lines.

3.4 Out-of-plane buckling

The out-of-plane buckling is one of the motivations for investigating the application of Kirigami cuts in the context of friction properties. Therefore, we perform a stretch simulation, at low temperature ($T = 5$ K) without any substrate, in order to verify that we can reproduce an out-of-plane buckling with the Tetrahedron and Honeycomb patterns intended for our study (see ??). For this investigation we consider the Tetrahedron (7, 5, 1) and the Honeycomb (2, 2, 1, 5) pattern in comparison to the non-cut sheet. We quantify the out-of-plane buckling by assessing the distribution of atoms along the z-direction (perpendicular to the plane) during stretching. We calculate the minimum and maximum z-value as well as the atom count quartiles 1%, 10%, 25%, 50% (median), 75%, 90% and 99% as shown in Fig. 3.9. The results show significant buckling for the Tetrahedron and Honeycomb patterns in comparison to the non-cut sheet which only exhibits minor buckling of ~ 2 Å which is on the same order as the lattice spacing. Moreover, we notice that the Tetrahedron pattern buckles more in consideration to the min. and max. peaks while the remaining quantiles seem to be more closely spaced than for the Honeycomb. By addressing the simulation results visually, using the *Open Visualization Tool OVITO*, we find that this can be attributed to fringes on the edge “flapping around” and thus increasing the min. and max. values.

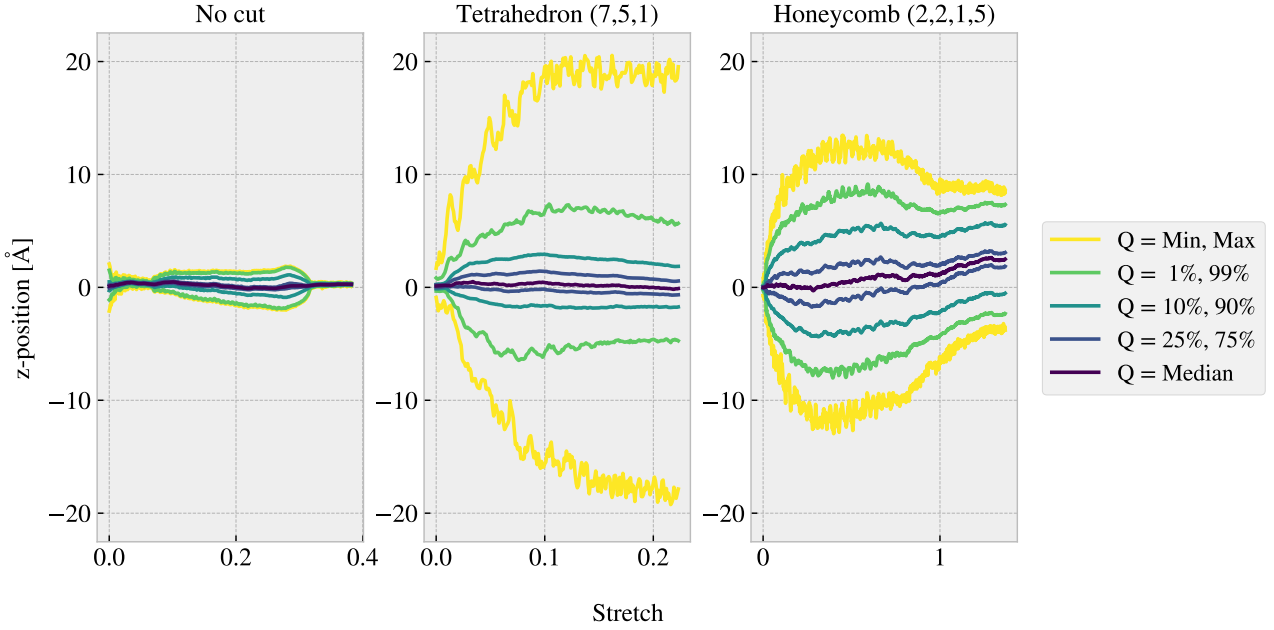


Figure 3.9: Out-of-plane buckling during stretching of the No cut, Tetrahedron (7, 5, 1) and Honeycomb (2, 2, 1, 5) sheet respectively in vacuum at low temperature $T = 5$ K. The buckling is measured by the distribution of the atom z-position (perpendicular to the sheet plane), for which the colors indicates selected quantiles. The yield strain were, reading from left to right, 0.38, 0.22 and 1.37.

Given the confirmation of out-of-plane buckling in a vacuum, as seen in Fig. 3.9, we reintroduce the substrate in order to investigate whether this effect carries over to a changing contact area. For this simulation we raise the temperature to the default value of $T = 300$ K. We keep the normal force off and let the sheet stick purely by the adhesion forces between the sheet and substrate. We quantify the contact area through the relative amount of atoms in the sheet within chemical range of the substrate. The cut-off for this interaction is set to 4 Å, inspired by [68], corresponding to $\sim 120\%$ the LJ equilibrium distance. Usually, the contact area is calculated as the number of contacting atoms multiplied by an associated area for each atom. However, since we are not interested in the absolute value of the area, but rather the relative change, we omit the multiplication factor. That is, we consider the relative number of atoms within the contact range, which is proportional to the contact area, as our metric of choice. The relative contact for the three configurations (No cut, Tetrahedron (7, 5, 1) and Honeycomb (2, 2, 1, 5)) during stretching are shown in figure Fig. 3.10. The figure reveals a significant drop in contact as the sheets are stretched, which agrees qualitatively with the buckling observed in Fig. 3.9 without the substrate. The Honeycomb pattern turns out to be both the most stretchable, with a rupture strain of 1.27, and the one with the biggest decrease in relative contact with a minimum of approximately 43%. Notice, that the relative contact is never actual 1.0 but instead reaches a maximum of 96% with no stretching. This is attributed to the temperature fluctuations and the choice of cut-off. Thus we might

Selected frames from the simulation result are shown in ?? which reveals a bit more information on how the buckling occurs. The Tetrahedron pattern deforms rather quickly and smoothly into small tetrahedron spikes, as the name suggests. In the Honeycomb pattern, on the other hand, the deformations initiate from one side first. As the sheet stretches more rows of the pattern are activated, producing the honeycomb-looking shape when seen from above. Both patterns exhibit a small increase in relative contact when they are approaching their yield strain, which agrees with the results from Fig. 3.9 where the buckling reduces slightly towards the rupture strain.

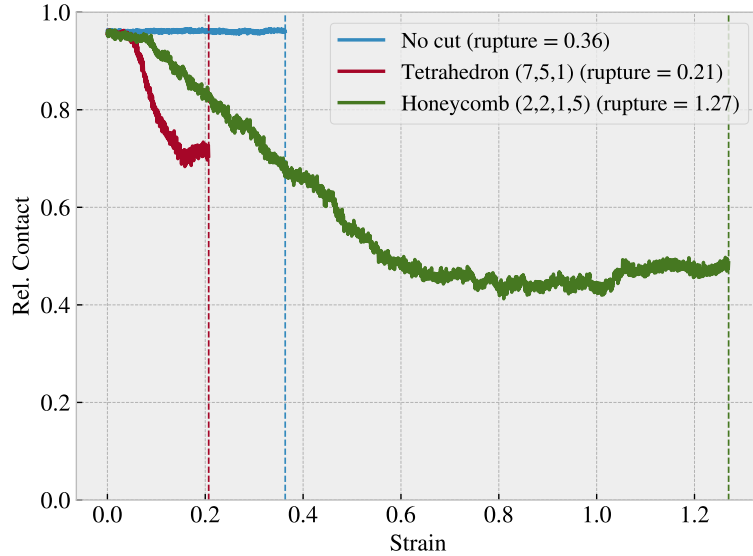


Figure 3.10: Relative contact, given as the relative number of atoms in the sheet being within chemical interaction range, vs. strain of the sheet. The cut-off for the interaction range is 4\AA corresponding to $\sim 120\%$ the LJ equilibrium distance. No normal force is applied and temperature is kept at $T = 300\text{ K}$.

Compare figure Fig. 3.10 to that of figure ?? where multiple simulations constitute the stretch-contact curve.

3.5 Investigating default parameters

We carry out a more extensive investigation of the friction dependence on temperature T , sliding speed v_{slide} , spring constant K , and timestep dt . This is done partly to understand how the dependencies relate to the theoretical, numerical and experimental results, and partly to understand how these parameters affect the stability of our system. We use the default parameters presented in Table 3.1 and investigate the results as we change parameters, one at a time. We keep the load at 1 nN . We consider the mean friction force, sampled from the last half of the simulation as described in Sec. 3.3, representing the kinetic friction. The results are shown in Fig. 3.11, where the shaded area (connected linearly) denotes the absolute error defined by the std as described in Sec. 3.3.

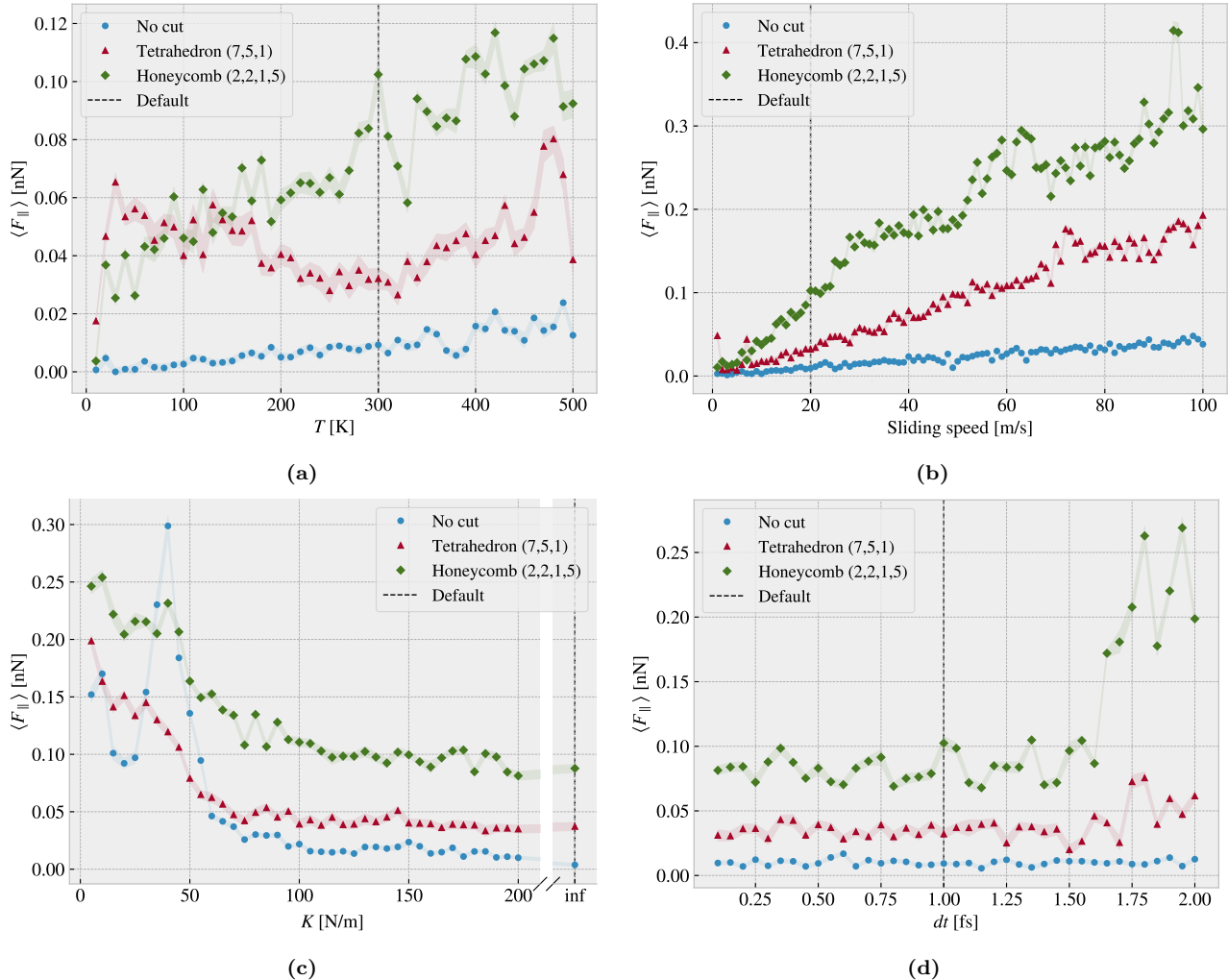


Figure 3.11: Main parameters investigation. Kinetic friction force

From the temperature investigation in Fig. 3.11a we find an increasing kinetic friction with temperature for both the non-cut sheet and the Honeycomb pattern. The Tetrahedron pattern shows both decreasing and increasing trends. The general trend shows a convex curve in the range (30–480 K) with a minimum around our default choice of 300 K, but with rapid fluctuations at the start (10–30 K) and end region (480–500 K). Similar fluctuations are also seen from the Honeycomb pattern, although it shows an underlying increasing trend throughout. When comparing the non-cut sheet and the Honeycomb pattern we observe that the slope for the increasing trend is high for the Honeycomb. From a theoretical and experimental point of view, we would expect a decrease in friction with temperature (see Sec. 2.5). However, an increasing trend is also observed in other MD simulation, for instance by Zhang et al. [75] sliding at 10 m/s, which is attributed to the high sliding speed associated with the ballistic motion. The default choice is initially based on the common choice of using the temperature $T = 300$ K. The non-cut and Tetrahedron friction seems to be rather stable around that point, but we do see some significant fluctuations for the Honeycomb pattern in this range. However, we do not regard this as a critical feature.

From the sliding speed investigation in Fig. 3.11b we generally find increasing friction with velocity. Due to the relatively high velocities used and the effects from the thermostat, we expect a viscous friction $F_k \propto v_{\text{sliding}}$ which matches rather well with these results. However, the Tetrahedron and Honeycomb sheets seem to fall slightly into a sublinear relationship as it approaches higher velocities. Furthermore, these sheets display indications of local fluctuations that could potentially be attributed to resonance effects, as discussed in relation to the phonon dynamics. Our choice of sliding speed at 20 m/s mainly reflects a consideration of computational cost, but the fact that no immediate resonance fluctuations appear in the proximity of this value supports the choice.

From the investigation of the spring constant parameter in Fig. 3.11c we observe a significant decrease in friction as the springs stiffen. This can be attributed to the transition from a stick-slip influenced regime to a smooth sliding regime as we saw for the force traces in Fig. 3.1. For soft springs the results are quite sensitive to the specific choice of spring constant which is especially seen for the non-cut sheet around $K = 40 \text{ N/m}$. Thus, in order to avoid this domain we settled for the infinitely stiff spring. This is also considered a more favorable option due to its ability to provide greater standardization of the simulations.

Finally, we consider the numerical stability of the result as we vary the simulation timestep in Fig. 3.11d. The general trend shows a stable plateau below $\sim 1.5 \text{ fs}$ for which higher values show signs of arising instabilities for the cut sheets (Tetrahedron and Honeycomb). This mainly confirms that our choice of timestep is within a reasonable range. However, we do see some fluctuations which are more significant for the cut sheets.

The observed fluctuations suggest that randomness plays a role in our simulations and also indicate that the cut sheets are relatively unstable. Further investigation through varying the random seed for the initial velocity and thermostat could shed more light on this matter. In the meantime, we may consider these fluctuations as a sign that the uncertainty in our results is higher than what was estimated using the running mean and running std evaluation. For the Honeycomb sheet, these fluctuations are on the order $\pm 0.017 \text{ nN}$.

3.5.1 Computational cost

We run the simulations on a CPU cluster made available by the University of Oslo. This allows us to run multiple simulations at once and with each simulation running in parallel on multiple CPU cores as well. As we decide on the simulation parameters we must also consider the computational cost. When selecting simulation parameters, we also need to keep in mind the computational cost. Given that the chosen parameters will be applied to multiple simulations, any increase in computational time will be multiplied by the number of intended simulations, which is expected to be around 10,000. The computational cost is especially dependent on the timestep and the sliding speed as this will affect the number of computations. As an extension of the analysis in Sec. 3.5 we report on the computational times associated with temperature, sliding speed, spring constant and dt. By retrieving the computational time used for the parameter investigation in Fig. 3.11 we get the timing as shown in Fig. 3.12. Note that these timings are only based on a single simulation for each parameter as opposed to an average over multiple runs which is necessary for more reliable data.

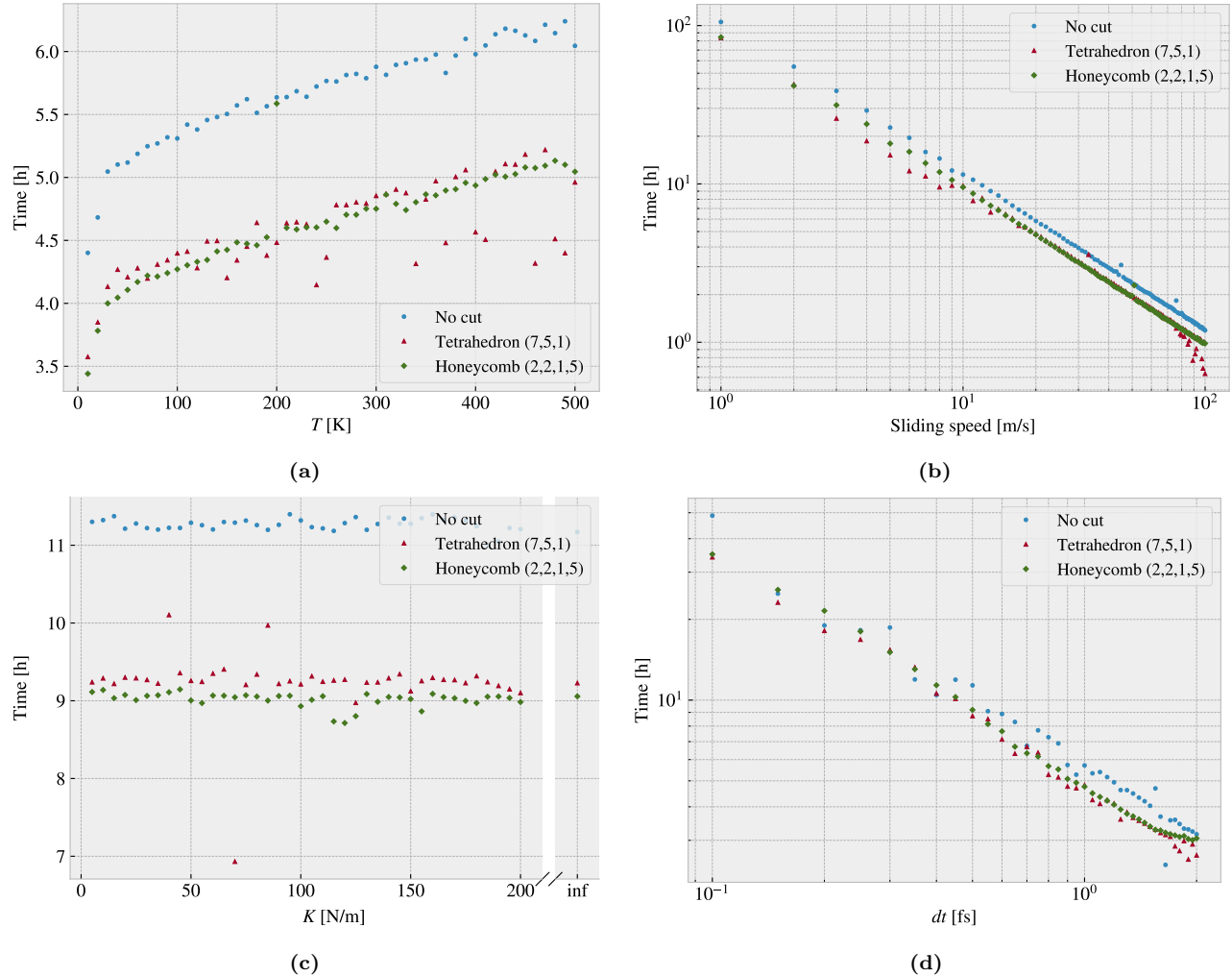


Figure 3.12: Computational cost related to temperature, sliding speed, spring constant and dt parameter in terms of CPU hours running on 16 cores on the cluster. Sliding speed follows $t \propto v^{-0.977 \pm 0.005}$ and dt follows $t \propto dt^{-0.87 \pm 0.02}$

The computational time is governed by the number of timesteps in the simulation and the time used per timestep. For a fixed sliding distance, the number of timesteps in the simulation are inversely proportional to sliding speed and similar inversely proportional to timestep dt . From the timings in Fig. 3.12 we find the sliding speed to obey this expectation rather well by $t \propto v^{-0.977 \pm 0.005}$ while the timing did not increase as strongly with timestep, falling below the $1/dt$ relation with $t \propto dt^{-0.87 \pm 0.02}$. Moreover, we find that increasing temperature also makes for an increased computation time. This can be attributed to an increase in the computation time associated with the force calculations. The rising temperature gives rise to more fluctuations in the system which might yield more atoms within the force calculation cutoffs for each computation. This kind of consideration can also be attributed to the reason for the deviating timing for dt . Finally, for the spring parameter, we did not see any noticeable effect on timing.

In general, we have selected our simulation parameters: temperature, sliding speed, spring constant, and timestep, based on numerical stability and computational cost. For the timestep, we found that a value of 1 fs, commonly used in similar studies [73, 74], produced stable results while higher values were prone to instabilities and lower values were computationally expensive. The sliding speed was chosen primarily based on computational cost, with a default value of 20 m/s being a reasonable compromise between computational efficiency and the lower values more commonly used in other studies. Although a lower sliding speed could lead to more commonly observed stick-slip motion, it represents a factor of 20 increase in computational time. Since stick-slip motion is out of reach based on the chosen sliding speed, we found that using an infinitely stiff spring $K = \infty$ was the

most reasonable option to ensure stable results. Finally, the temperature investigation did not provide much guidance for a specific choice, so we settled for the standard choice of room temperature $T = 300\text{ K}$.

3.6 Load and stretch dependencies

So far, we have carried out a general analysis of the system behavior under the influence of various simulation parameters. This lays the foundation for the remaining study as we now shift our intention towards the friction dependence of strain and load.

3.6.1 Pressure reference for normal load

We consider a load range of $0.1\text{--}10\text{ nN}$ which coincide with the general investigated range in other MD studies [68, 74]. In order to relate the magnitude of this load we provide a short calculation of the corresponding pressure. We will use the pressure underneath a stiletto-heeled shoe as a high-pressure reference from our macroscale perspective. The diameter of a stiletto-heeled shoe can be less than 1 cm [84], and hence an 80 kg man³ standing on one stiletto heel, with all the weight on the heel, will correspond to a pressure

$$P = \frac{F}{A} = \frac{mg}{r^2\pi} = \frac{80\text{ kg} \cdot 9.8 \frac{\text{m}}{\text{s}^2}}{\left(\frac{10^{-2}\text{ m}}{2}\right)^2\pi} = 9.98 \text{ MPa.}$$

The fact that the pressure under a stiletto heel can get this high, actually greater than the pressure under an elephant foot, is an interesting realization in itself that is often used in introductory physics courses [85], but this also serves as a reasonable upper bound for human executed pressure. With a full sheet area of $\sim 21 \times 10^3 \text{ \AA}^2$ our load range of $0.1\text{--}10\text{ nN}$ corresponds to a pressure of $0.47\text{--}47\text{ MPa}$ which relates nicely to our macroscale reference. This pressure might be incompatible with various industrial purposes, but with no specific application in mind, this serves as a decent reference point. Notice, that if we consider a human foot with area 113 cm^2 [86] the pressure drops to a mere 70 kPa corresponding to only $\sim 0.01\text{ nN}$.

3.6.2 Strain dependency

We consider the effects of stretching the sheet using the non-cut, Tetrahedron (7, 5, 1) and Honeycomb (2, 2, 1, 5) sheet as used so far. For each configuration, we run a rupture test where the given sheet is stretched under zero load, but still under the influence of adhesion from the substrate. The rupture strain is then recorded, and multiple new simulations are initiated with strain values between zero and the rupture strain. For the sampling of the stretch values in the available range, we use a pseudo-uniform distribution, meaning that we divide the given interval into equal segments and pick a value from each segment by a uniform distribution. This is due to numerical limitations in LAMMPS⁴, but we find that this gives evenly spaced values which also carry some randomness. For the load we use 0.1 , 1 and 10 nN .

First, we aim to reproduce the contact investigation from Fig. 3.10. We quantify the relative contact as described in Sec. 3.4, but we convert this into a single metric for a given simulation by considering the average of the last 50% of data points, similar to what we have done for the mean friction. We also adopt a similar method for quantifying the error (see Sec. 3.3). The results are shown in Fig. 3.10 where we observe a significant decrease in relative contact for the kirigami patterns which qualitatively agrees with the non-loaded continuous stretch simulation in Fig. 3.10. This result implies that the change in contact is not governed by a momentum effect during stretching, as each simulation now keeps the strain constant throughout the simulation. The absolute error for the mean rel. contact was generally quite low on the order of 0.01 for all configurations.

From an asperity theory point of view, this reduction in contact is theorized to induce a similar reduction in friction. However, when considering the kinetic friction in Fig. 3.13b we find that this is not the case. For the Tetrahedron and Honeycomb patterns, we find that the friction initially increases with a decreasing contact

³Yes, a man can certainly wear stiletto heels.

⁴In LAMMPS, we sample the various strain values by storing restart files during the straining of the sheet. The restart values are stored at specific timesteps governed by a LAMMPS variable. Such variables allow for a vector of uniform randomly chosen values, but unfortunately, we are not able to sort the vector for ascending values. This will lead to the script waiting to store each restart file according to the timesteps in the unsorted vector. As soon as the next timestep value is less than the current timestep the program will stop producing restart files and thus skip most of them. However, by first defining a series of intervals we can draw a uniform number for each interval without getting into trouble.

area. Yet, these are not simply inversely proportional as the friction force suddenly dips down and up again, in the strain range of 0.08–0.11 for the Tetrahedron and 0.73–1.05 for the Honeycomb pattern. When considering the non-cut sheet, we find that both the contact area and friction remain seemingly unaffected by strain. This indicates that the contact area is not a dominating mechanism for friction in our system, but the underlying mechanism might make for a correlation between a decreasing contact area and the non-linear friction-strain curve observed here. The latter point can be supported by the fact that the contact-strain and friction-strain curve both show signs of a discontinuous jump around a strain of 0.32. Since the non-cut sheet exhibits a flat friction-strain profile we cannot attribute the behavior to an increased tension either. The friction effect of tension of a graphene sheet has been investigated by Zhang et al. [65]. However, they report a decreasing friction with tension which qualitatively contradicts our observation as the direction of the effect is opposite. Instead, we might point to a commensurability effect or perhaps a change in the structural stiffness which is reported as an important feature by [30]. We observe that the initial friction value of the non-strained sheet varies across configurations, with the initial friction increasing from the non-cut sheet, through the Tetrahedron sheet, to the Honeycomb sheet. This is more evident from the parameter investigation from Fig. 3.11, but the size of this effect is within a range on the order of [0.01, 0.1] nN. We notice also that the two orders of magnitude increase in normal load did not make a significant difference in the results. The estimated absolute error marked by a shaded area in Fig. 3.13b were fairly low for both friction on the order 10^{-3} nN and relative contact on the order of 10^{-4} .

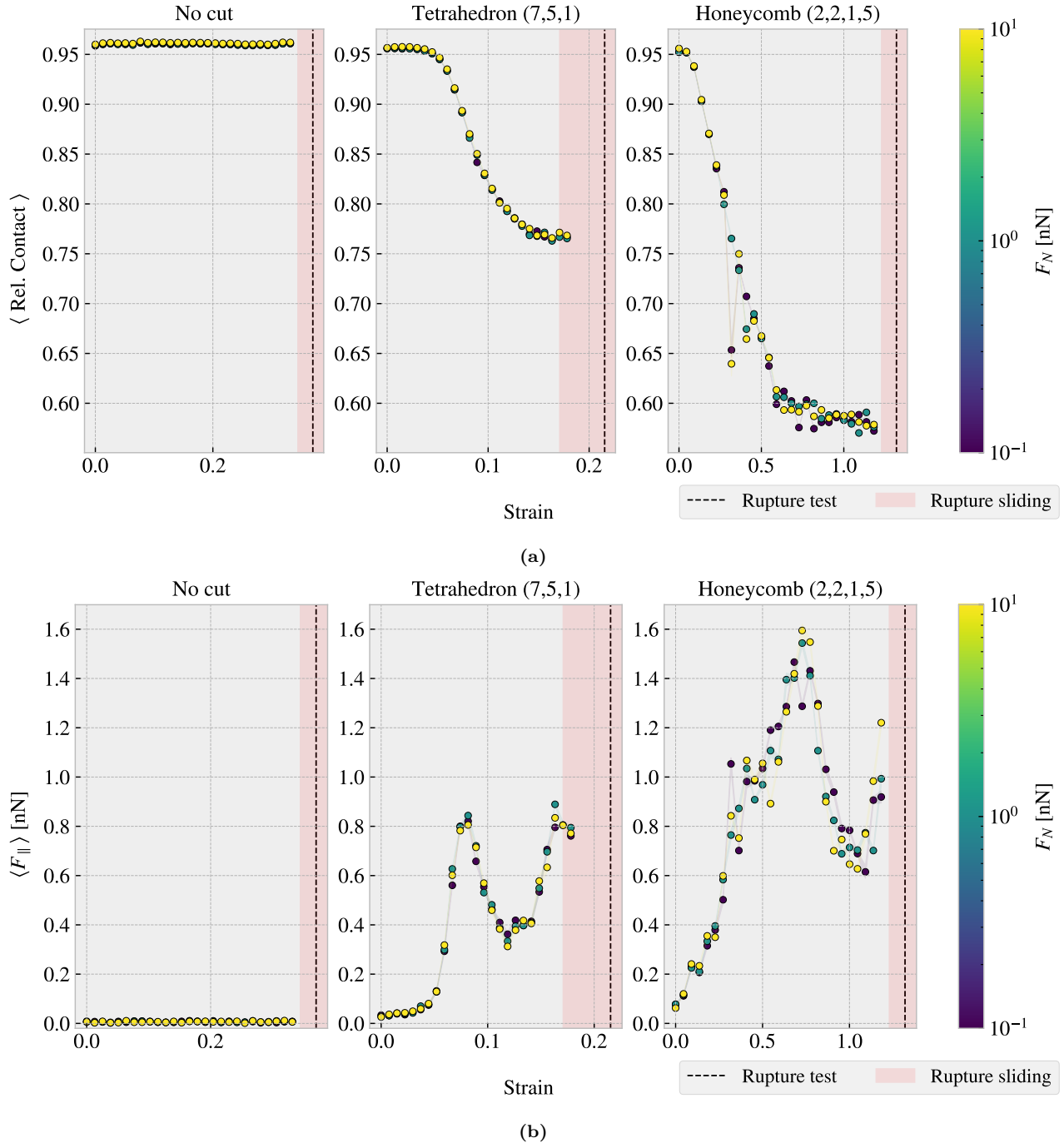


Figure 3.13: Average relative contact and average friction for multiple simulations, consisting of 30 stretch values sampled from a pseudo uniform distribution between 0 and the rupture point in combination with loads 0.1, 1 and 10 nN, for each of the configurations: non-cut, Tetrahedron (7,5,1) and Honeycomb (2,2,1,5). The average is taken over the last half of the sliding phase. The red shade denotes the stretch range where ruptures accoured during sliding while the black-dotted line represent the rupture point in the no load rupture test. (a) The average relative contact defined as the relative number of atoms within a contact threshold of 4 Å to the substarte. The absolute error is on the order 0.01 (b) The average mean friction force parallel to the sliding direction. The absolute error for the mean friction is on the order 0.001–0.01 nN. Mention error for contact being on the order e-4–e-5

By considering the increase in friction from zero strain towards the first peak of the friction-strain curve we find that the Tetrahedron pattern exhibits a relative friction increase of ~ 27.7 while the Honeycomb pattern

exhibits a relative increase of ~ 22.4 . This is in itself a remarkable result, but considering that the friction drops almost as dramatically afterward makes for an even more unexpected behavior. For the Tetrahedron sheet the friction drops by ~ 0.51 nN during an increased strain $\Delta\varepsilon \sim 0.04$ while Honeycomb drops ~ 0.98 nN during a strain increase of $\Delta\varepsilon \sim 0.36$. These results are promising for the aim of demonstrating a negative friction coefficient for a system with coupled load and stretch. We will discuss this further at the end of this chapter in Sec. 3.6.4.

3.6.3 Load dependency

From the investigation of the stretch dependency we saw that increasing the normal load from 0.1 to 10 nN did not make a considerable impact on the friction in comparison to the effect associated with strain. One special feature of our system is that we only apply load to the pull blocks, and thus one might suspect this to be of importance. Therefore, we investigate the friction under varying loads for a non-cut sheet comparing the case of loading the pull block against a more traditional uniform loading of the sheet as shown in Fig. 3.14. Both load distributions show a seemingly non-dependent relationship between friction and load considering the size of our estimated error. Nonetheless, we do not see any indications that the uniform loading changes the qualitative behavior.

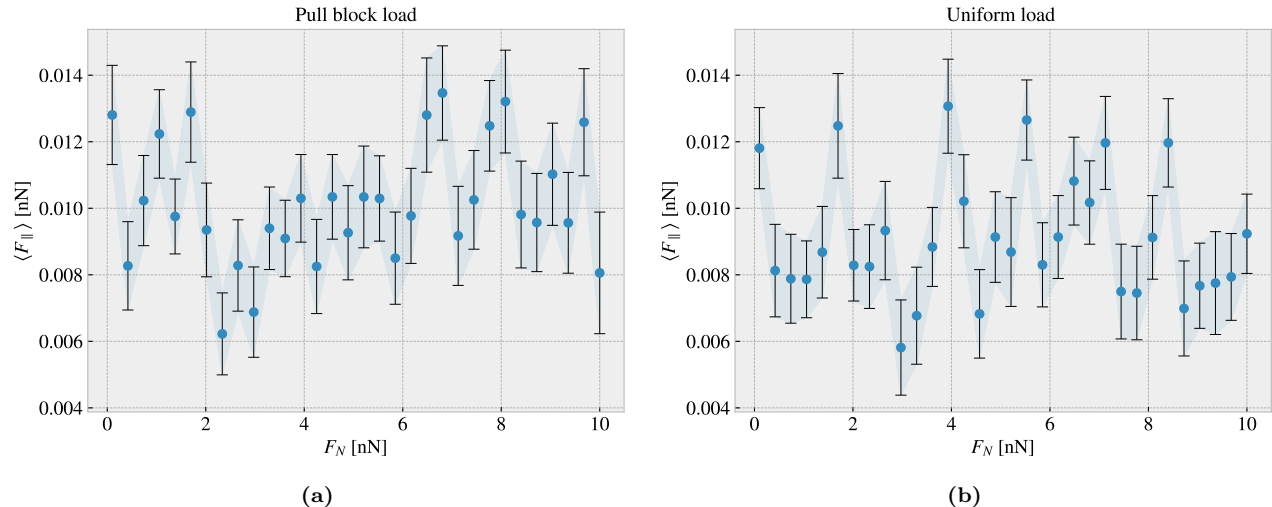


Figure 3.14: Multiple simulations of non-cut sheet under different load. Mean friction is plotted against load for two different variations of loading distribution. (a) Normal loading is applied to the pull blocks. (b) Normal loading is applied uniformly to the sheet.

In order to further investigate the friction dependency of normal load for the Kirigami patterns as they are stretched, we select a subset of stretch stages from Fig. 3.13b and perform additional simulations with a logarithmically increasing normal load in the extended load range 0.1–100 nN, using 30 load data points for each strain. The results are shown in Fig. 3.15. When spanning three orders of magnitude for the normal load we find some increase in friction with load. This goes for all patterns, but it is only really visible for the non-cut sheet as the values on the friction axis show a more narrow range. Notice that the load is plotted for a logarithmic axis which makes any seemingly linear trends on the figure sublinear. However, as the normal load approaches 100 nN we do start to see an increase that is more reminiscent of a linear relationship, but this is difficult to judge given that the change in friction is small in comparison to the noise in the data. Note that we omitted the error bars for visual purposes but they are on the same order of magnitude as shown in Fig. 3.14.

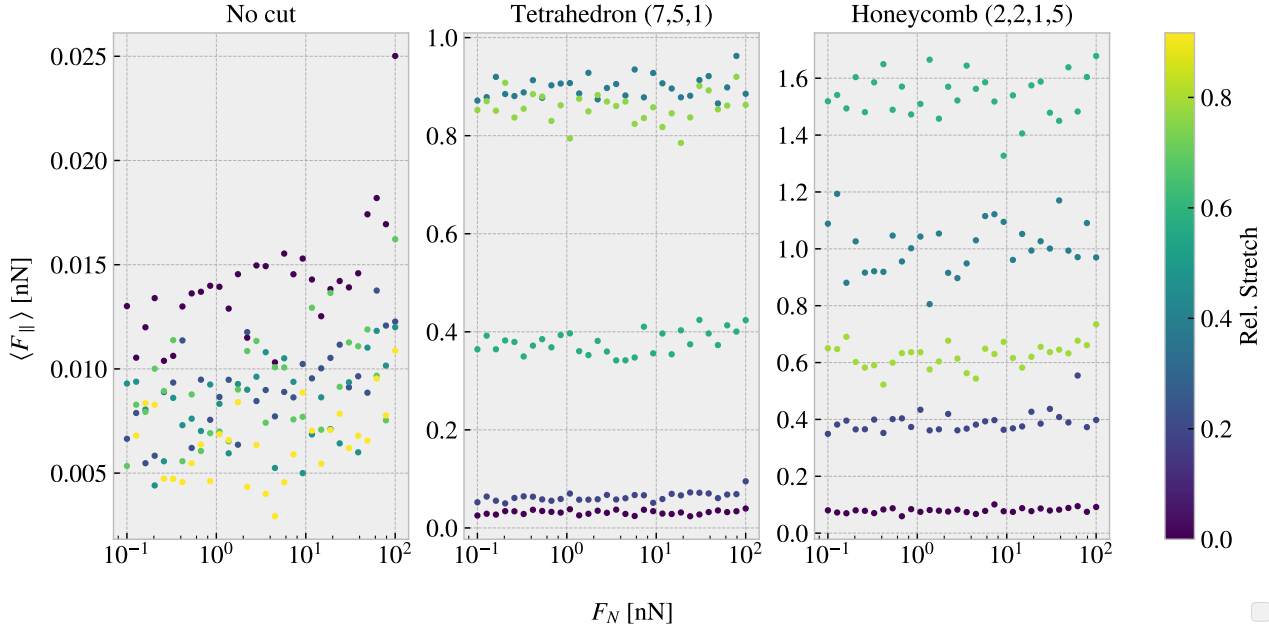


Figure 3.15: Mean friction force vs. load in the range 0.1–100 nN, for the non-cut, Tetrahedron (7, 5, 1) and Honeycomb (2, 2, 1, 5) sheet resepectively, at different stretch stages relative to their rupture point.

From the friction measurements in Fig. 3.15 we see that the non-cut sheet generally produces a friction force in the order of 0.005–0.0025 nN throughout the 0.1–100 nN load range. Using a ratio based friction coefficient definition Eq. (2.2a), $\mu_1 = F_{\text{fric}}/F_N$, this would lead to a coefficient roughly in the range

$$\mu_1, \text{ Eq. (2.2a): } \text{No cut} \sim [10^{-4}, 0.13], \quad \text{Tetrahedron} \sim [4 \times 10^{-4}, 8.7], \quad \text{Honeycomb} \sim [9 \times 10^{-4}, 15.2].$$

However, these values mainly reflect the poorness of this definition, as we find the values to diverge at low load and decrease towards high load due to the lacking linear relationship and an offset in the load curve corresponding to a finite friction at zero load. This offset is drastically enhanced for the Kirigami patterns under strain. Due to the small changes in friction compared to the noise in the data, it is not sensible to calculate the slope dF_{fric}/dF_N as a function of load. Nonetheless, if we force a linear fit for the whole range and use the second definition Eq. (2.2b) as $\langle \mu_2 \rangle = \Delta F_{\text{fric}}/\Delta F_N$, we get average coefficients in the range

$$\mu_2, \text{ Eq. (2.2b): } \text{No cut} \sim [4, 9] \times 10^{-5}, \quad \text{Tetrahedron} \sim 5 \times [10^{-5}, 10^{-4}], \quad \text{Honeycomb} \sim [1, 9] \times 10^{-4},$$

depending on the strain values. These numbers should be interpreted cautiously, but we can take it as a rough estimate of the friction coefficient being on the order 10^{-4} – 10^{-5} . This relates to the finding by [57] who reported a seemingly non-existing relationship between friction and normal load with change in friction that corresponds to friction coefficients in the range 10^{-3} – 10^{-4} when using the slope definition Eq. (2.2b). This supports the idea that the graphene sheet does in fact exhibit superlubric behavior in these conditions. Moreover, the fact that the increase with load is relatively unaffected by the stretching points to the fact that the strain-induced effect mainly shifts the load curve towards higher friction but does not significantly alter its slope.

3.6.4 Prospects of a negative friction coefficient

Considering the results from Sec. 3.6.2 and Sec. 3.6.3 we find that strain-induced friction effects, on the order of $/SI1nN$, are generally dominating in comparison to load-induced effects on the order of 0.01 nN given a load range of 10^2 nN. This is promising for the idea of achieving a negative friction coefficient for a nanomachine system that couples load and strain. By applying load on the nanomachine we would increase both the load and the strain on the sheet simultaneously. However, since the friction dependency to strain dominates in comparison to load effects such a system can be designed entirely by considering the strain dependency. The friction coefficient is by our definition (Eq. (2.2b)) given as the slope of the friction F_f vs. normal force F_N curve.

Hence, for two points $\{(F_{N,1}, F_{f,1}), (F_{N,2}, F_{f,2})\}$, $F_{N,1} < F_{N,2}$ we can evaluate the associated friction coefficient $\mu_{1,2}$ as

$$\mu_{1,2} = \frac{F_{f,2} - F_{f,1}}{F_{N,2} - F_{N,1}} = \frac{\Delta F_f}{\Delta F_N}.$$

If we neglect load effects $F_f(F_N, \varepsilon) \sim F_f(\varepsilon)$ and consider a coupling $\varepsilon = RF_N$ with linear coupling ratio R we get

$$\mu_{1,2}(\varepsilon_1, \varepsilon_2) = \frac{\Delta F_f(\varepsilon_1, \varepsilon_2)}{\frac{1}{R}(\varepsilon_2 - \varepsilon_1)} = R \frac{\Delta F_f(\varepsilon_1, \varepsilon_2)}{\Delta \varepsilon}. \quad (3.1)$$

When considering the ratios found for the reduction in friction with strain for the Tetrahedron and Honeycomb patterns in Sec. 3.6.2 we find the corresponding coupled system friction coefficients to be

$$\text{Tetrahedron: } R \frac{-0.51 \text{ nN}}{0.04} = -R \cdot 12.75 \text{ nN}, \quad \text{Honeycomb: } R \frac{-0.98 \text{ nN}}{0.36} = -R \cdot 2.72 \text{ nN} \quad (3.2)$$

This showcases that we might be able to utilize the strain effect to achieve a negative friction for the system of coupled strain and load

Chapter 4

Summary

In this thesis we have studied nanoscale friction of a Kirigami graphene sheet under the influence of load and strain using MD simulations. We have developed a numerical framework for generating various Kirigami designs which was used to create a dataset of the frictional behavior depending on the Kirigami pattern, strain and loading. Our findings suggest that the frictional behavior of a Kirigami sheet is highly dependent on the geometry of the pattern and the strain conditions. We observed that the out-of-plane buckling can be associated with a non-linear friction-strain curve which can be utilized to demonstrate a negative friction coefficient in a system with coupled load and strain. Moreover, we have investigated the possibility to use machine learning on this dataset and attempted an accelerated search. Our result suggest that machine learning can be feasible for this approach, but more data is needed to provide a more reliable foundation for a search of new Kirigami patterns. In this chapter we will summarize the findings in more detail and draw some conclusions. At the end we will provide some topics for further research.

4.1 Summary and conclusions

4.1.1 Designing an MD simulation

We have designed an MD simulation for the examination of friction for a graphene sheet sliding on a silicon substrate. The key system features were the introduction of the pull blocks, defined as the end regions of the sheet with respect to the sliding direction, which was utilized for applying normal load and sliding the sheet. The pull blocks were made partly rigid and used to employ a thermostat as well. By an analysis of the friction forces retrieved from sliding simulations we defined a standardized metric for kinetic friction. We measured the force acting from the substrate on the full sheet (including the pull blocks) with respect to the sliding direction and defined kinetic friction by the mean value of the last half of the simulation. The uncertainties were estimated on the basis of the fluctuations in the running mean. We found that the assessment of static friction was ambiguous for our simulation and did not pursue this further. From the analysis of the force traces, friction force vs. time, we identify the friction behavior in our simulation domain as being in the smooth sliding regime mainly due to the choice of sliding speed (20 m/s) and infinitely stiff springs. This was further supported by a demonstration of a transition to stick-slip behavior with softer springs and a lowering of sliding speed. By conducting a more systematic investigation of the effects of temperature, sliding speed, spring constant and timestep, we settled on the default values based on numerical stability and computational cost. We found that friction increased with temperature which we attribute to being in the ballistic sliding regime. We used the room temperature 300 K as a standard choice. Furthermore, we found friction to increase with velocity as expected, with some signs of phonon resonance at certain sliding speeds as well. We chose a rather high velocity of 20 m/s mainly for the consideration of computational costs. For the spring constant, we found decreasing friction with increasing stiffness of the springs which is associated with the transition from a stick-slip-influenced regime toward smooth sliding. The choice of an infinitely stiff spring was made from a stability assessment. Finally, we confirmed that a timestep of 1 fs provides reasonable numerical stability. However, based on fluctuations with timestep we find that the uncertainty in the simulations might be higher than first estimated.

4.1.2 Generetig Kirigami patterns

In order to investigate the effects of Kirigami design we have created a numerical framework for generating various patterns. By defining an indexing system for the hexagonal lattice structure we were able to define the Kirigami designs as a 2D binary matrix for numerical implementation. We digitalized two different macroscale designs, which we named the *Tetrahedron* and *Honeycomb* pattern, that successfully produced out-of-plane buckling when stretched. Through our numerical framework we were able to create an ensemble of perturbed unique variations which yielded approximately 135k and 2025k for the Tetrahedron and Honeycomb patterns respectively. When considering the possibility to translate the patterns we find the ability to increase the number by roughly a factor 100. In addition we created a framework for generating random walk based Kirigami patterns. This was regulated by introducing features such as bias, avoidance of existing cuts, preference to keeping a direction and procedures to repairing the sheet for simulation purposes. In general, the capabilities of the numerical framework for generating Kirigami designs exceeded our computational resources with regard to performing MD simulation under different load and strain for each of the designs. Thus our MD-based dataset only utilized a subset of configurations with 9660 data points based on 216 Kirigami configurations (Tetrahedron: 68, Honeycomb: 45, Random walk: 100, Pilot study: 3). Thus our Kirigami generative framework can be valuable for further studies on an extended dataset.

4.1.3 Control friction using Kirigami

We have investigated the frictional behavior of the Tetrahedron and Honeycomb patterns in comparison to a non-cut sheet under various strains and loads. Initially, we observed that straining the Kirigami sheets in vacuum resulted in an out-of-plane buckling. When adding the substrate to the simulation this translated into a decreasing contact area with strain. We found the Honeycomb sheet to exhibit the most significant buckling with a corresponding reduction of relative contact area to approximately 43%. The non-cut sheet did not produce any significant buckling in comparison. We found that friction generally increased with strain which contradicts the asperity theory hypothesis of decreasing friction with decreasing contact area. Moreover, the friction-strain curve exhibited highly non-linear trends with strong negative slopes (see Fig. 3.13), while the non-cut sheet did not show any significant dependency on the strain. We also found that the non-stretched Kirigami patterns did affect friction to some degree, but this was one order of magnitude lower than the effects associated with the strain in combination. This led us to the conclusion that the changing contact area cannot be regarded as a dominant mechanism for friction in the Kirigami sheet system nor the independent consideration of sheet configuration or tension in the sheet. When considering the dependency with load we generally found a weak dependency which can be associated with a friction coefficient on the order of 10^{-4} – 10^{-5} even though we could not confirm any clear relationship. This is best attributed to a superlubric state of the graphene sheet as seen in other studies as well. The slope of the friction-load curves was not considerably affected by the straining of the Kirigami sheet which led us to the conclusion that the strain-induced effects are dominant in comparison to any load-related effects. By proposing a linear coupling between load and strain with ratio R we find that these results suggest the possibility to find negative friction coefficients in certain load ranges following $-R12.75\text{ nN}$ for the Tetrahedron and $-R \cdot 2.72\text{ nN}$ for the Honeycomb pattern.

4.1.4 Capture trends with ML

With the use of MD simulations, we have generated an extended dataset of 9660 data points based on 216 Kirigami configurations (Tetrahedron: 68, Honeycomb: 45, Random walk: 100, Pilot study: 3) under various strains and normal loads. The dataset reveals some general correlations with mean friction, such as a positive correlation to strain (0.77) and porosity (0.60), and a negative correlation to contact area (-0.67). These results align with the findings from the pilot study suggesting that these features are relevant, but not necessarily the cause, of the observed phenomena. By defining the friction property metrics: $\min F_{\text{fric}}$, $\max F_{\text{fric}}$, $\max \Delta F_{\text{fric}}$ and $\max \text{drop}$ (maximum decrease in friction with strain), we investigated the top candidates within our dataset. From these results, we found no incentive of the possibility to reduce friction with the Kirigami approach since the non-cut sheet provided the lowest overall friction. Regarding the maximum properties, we found an improvement from the original pilot study values and with the Honeycomb pattern producing the highest scores. This suggests that the data contains some relevant information for optimization with respect to these properties. Among the top candidates, we found that a flat friction-strain profile is mainly associated with little decrease in the contact area and vice versa.

For the machine learning investigation, we have implemented a VGGNet-16-inspired convolutional neural network with a deep “stairlike” architecture: C32-C64-C128-C256-C512-C1024-D1024-D512-D256-D128-D64-D32, for convolutional layers C with the number denoting channels and fully connected (dense) layers D with the number denoting nodes. The final model contains 1.3×10^7 and was trained using the ADAM optimizer for a cyclic learning rate and momentum scheme for 1000 epochs while saving the best model during training based on the validation score. The model validation performance gives a mean friction R^2 score of $\sim 98\%$ and a rupture accuracy of $\sim 96\%$. However, we got lower scores for a selected subset of the Tetrahedon ($R^2 \sim 88.7\%$) and Honeycomb ($R^2 \sim 96.6$) pattern based on the top 10 max drop scores respectively. These scores were lower despite the fact that the selected set was partly included in the training data as well and the fact that the hyperparameter selection favored the performance on this selected set. Thus we conclude that these selected configurations, associated with a highly non-linear friction-strain curve, represent a bigger challenge for machine learning prediction. One interpretation is that these involve the most complex dynamics and perhaps that this is not readily distinguished from the behavior of the other configurations which constitutes the majority of the data set. By evaluating the ability for the model to rank the dataset according to the property scores we found in general a good representation of the top 3 scores for the maximum categories, while the minimum friction property ranking was lacking. We attribute this latter observation to a higher need for precision in order to rank the lowest friction values properly which the model did not possess.

In order to provide a more true evaluation of the model performance we created a test set based on MD simulations for an extended Random walk search. This test revealed a significantly worse performance than seen for the validation set with a two-order of magnitude higher loss and a negative friction mean R^2 score which corresponds to the prediction being worse than simply guessing on a constant value based on the true data mean. However, by considering one of the early hypertuning choices, regarding architecture complexity, we evaluated the model when prioritizing mainly for the lowest validation loss. This gave similar performance on the test set which indicates that it is not simply a product of a biased hypertuning process, since we based our choices on the selected configuration set (which overlapped with the training data). Instead, it points to the fact that our original dataset did not cover a wide enough configuration distribution to accurately capture the full physical complexity of the Kirigami friction behavior.

4.1.5 Accelerated search

Using the ML model we performed two types of accelerated search. One by evaluating the property scores of an extended dataset and another with the use of the genetic algorithm approach. For the extended dataset search we used the developed pattern generators to generate $135\text{ k} \times 10$ Tetrahedon, $2025\text{ k} \times 10$ Honeycomb and 10 k Random walk patterns. For the minimum friction property, the search suggests a favoring of a low cut density (low porosity) which aligns with the overall idea that the dataset does not provide an incentive for further friction reduction. The maximum properties resulted in some minor score increases but the suggested candidates were overlapping with the original dataset. By investigating the sensitivity to translation of the Tetrahedron and Honeycomb patterns we found that the model predictions varied drastically with pattern translation. This can be attributed to a physical dependency since the edge of the sheet is effected by this translation. However, due to the poor model performance on the test set, we find it more likely to be a model insufficiency arising from a lacking training dataset.

For the genetic algorithm approach, we investigated the optimization for the max drop property with respect to starting population based on the result from the extended dataset accelerated search, and some random noise initializations with different porosity values. This approach did not provide any noteworthy incentive for new design structures worth more investigation. In general, the initialization of the population itself proved to be a more promising strategy than the genetic algorithm. However, this is highly affected by the uncertainty of the model predictions, and thus we did not pursue this any further. By considering the Grad-CAM explanation method we found that the model predictions sometimes seem to pay considerable attention to the top and bottom edge of the configurations. This is surprising since these are not true edges but are connected to the pull blocks in the simulation. Despite the uncertainties in the predictions, we argue that this might be attributed to thermostat effects from the pull blocks and thus we note this as a feature worth more studying.

4.1.6 Negative friction coefficient

By enforcing a coupling between load and stretch, mimicking a nanomachine attached to the sheet, we investigated the load curves arising from loading of the Tetrahedron (7, 5, 1) and Honeycomb (2, 2, 1, 5) pattern from the pilot study. The non-linear trend observed for increasing strain carried over to the coupled system as well producing a highly non-linear friction-load curve. This demonstrates a negative friction coefficient [say something about the values.](#)

4.2 Outlook / Perspective

Having successfully demonstrated a non-linear effect on friction with increasing strain of the sheet our results invite a series of further studies to investigate this relation. First of all, it would be valuable to investigate how the friction-strain curve depend on temperature, sliding speed, spring constant, and on load for an increased range $F_N > 100nN$. This is especially interesting in the context up conditions leading to a stick-slip behavior as our results were carried in the smooth sliding. Moreover, it would be important to verify that the choices for relaxation time and pauses are not critical for the qualitative observations as well as trying a different interatomic potential for the graphene and perhaps an entirely different substrate material. Especially the Adaptive Intermolecular Reactive Empirical Bond Order (AIREBO) potential for the modeling of the graphene sheet might be of interest. The effects from excluding adhesion (the LJ interaction) can also be useful for the investigation of the observed phenomena.

In order to get a better understanding of the underlying mechanism for the friction-strain relationship we might investigate commensurability effects further by varying the scan angle. We might also consider investigating the friction-strain relationship under a uniform load to get insight into whether the loading distribution is of importance. Another topic worth studying is the relation to scale. Thus it would be interesting to study size effects but also further look into edge effects by translating the pattern. With this regard, we would also suggest a more detailed study of the effect from the thermostat in the pull blocks which is suggested to have a possibly importance by judging from the machine learning model Grad-CAM analysis.

For machine learning, we can either try to extend the data set to resolve the issue of the model not being generalized enough. We can also create a dataset for a single kirigami design and include some of the mentioned physical variables above and attempt to use machine learning for unraveling these relations. In that context we would advice for a more detailed investigation of machine learning techniques. If successful this would invite a study of inverse design methods such as GAN or diffusion models.

- How is this behavior effected by scaling?
- How does the distribution of normal load effect the Kirigami friction behavior?
- Things to vary: load range, scan directions, adhesive forces, longer relaxation time, different potential (AIREBO)
- Investigate if the contact area is effecting the friction non-linear by turning of friction force for atoms corresponding to those that lift off from the sheet during the out-of-plane buckling.
- Investigations of commensurability effects.
- Study dependency of translation of the patterns as suggested by the ML results.
- Investigate effects from pull blocks...
- Investigate effects from the thermostat since the top and bottom edges was shown interest by the model prediction.

Appendices

Appendix A

Appendix A

Appendix A

Appendix B

Appendix B

Appendix C

Bibliography

- ¹E. Gnecco and E. Meyer, *Elements of friction theory and nanotribology* (Cambridge University Press, 2015).
- ²Bhusnur, “Introduction”, in *Introduction to tribology* (John Wiley & Sons, Ltd, 2013) Chap. 1, 1–?
- ³H.-J. Kim and D.-E. Kim, “Nano-scale friction: a review”, *International Journal of Precision Engineering and Manufacturing* **10**, 141–151 (2009).
- ⁴K. Holmberg and A. Erdemir, “Influence of tribology on global energy consumption, costs and emissions”, *Friction* **5**, 263–284 (2017).
- ⁵B. Bhushan, “Gecko feet: natural hairy attachment systems for smart adhesion – mechanism, modeling and development of bio-inspired materials”, in *Nanotribology and nanomechanics: an introduction* (Springer Berlin Heidelberg, Berlin, Heidelberg, 2008), pp. 1073–1134.
- ⁶P. Z. Hanakata, E. D. Cubuk, D. K. Campbell, and H. S. Park, “Accelerated search and design of stretchable graphene kirigami using machine learning”, *Phys. Rev. Lett.* **121**, 255304 (2018).
- ⁷P. Z. Hanakata, E. D. Cubuk, D. K. Campbell, and H. S. Park, “Forward and inverse design of kirigami via supervised autoencoder”, *Phys. Rev. Res.* **2**, 042006 (2020).
- ⁸L.-K. Wan, Y.-X. Xue, J.-W. Jiang, and H. S. Park, “Machine learning accelerated search of the strongest graphene/h-bn interface with designed fracture properties”, *Journal of Applied Physics* **133**, 024302 (2023).
- ⁹Y. Mao, Q. He, and X. Zhao, “Designing complex architected materials with generative adversarial networks”, *Science Advances* **6**, eaaz4169 (2020).
- ¹⁰Z. Yang, C.-H. Yu, and M. J. Buehler, “Deep learning model to predict complex stress and strain fields in hierarchical composites”, *Science Advances* **7**, eabd7416 (2021).
- ¹¹A. E. Forte, P. Z. Hanakata, L. Jin, E. Zari, A. Zareei, M. C. Fernandes, L. Sumner, J. Alvarez, and K. Bertoldi, “Inverse design of inflatable soft membranes through machine learning”, *Advanced Functional Materials* **32**, 2111610 (2022).
- ¹²S. Chen, J. Chen, X. Zhang, Z.-Y. Li, and J. Li, “Kirigami/origami: unfolding the new regime of advanced 3D microfabrication/nanofabrication with “folding””, *Light: Science & Applications* **9**, 75 (2020).
- ¹³Z. Deng, A. Smolyanitsky, Q. Li, X.-Q. Feng, and R. J. Cannara, “Adhesion-dependent negative friction coefficient on chemically modified graphite at the nanoscale”, *Nature Materials* **11**, 1032–1037 (2012).
- ¹⁴B. Liu, J. Wang, S. Zhao, C. Qu, Y. Liu, L. Ma, Z. Zhang, K. Liu, Q. Zheng, and M. Ma, “Negative friction coefficient in microscale graphite/mica layered heterojunctions”, *Science Advances* **6**, eaaz6787 (2020).
- ¹⁵D. Mandelli, W. Ouyang, O. Hod, and M. Urbakh, “Negative friction coefficients in superlubric graphite–hexagonal boron nitride heterojunctions”, *Phys. Rev. Lett.* **122**, 076102 (2019).
- ¹⁶R. W. Liefferink, B. Weber, C. Coulais, and D. Bonn, “Geometric control of sliding friction”, *Extreme Mechanics Letters* **49**, 101475 (2021).
- ¹⁷N Manini, O. M. Braun, E Tosatti, R Guerra, and A Vanossi, “Friction and nonlinear dynamics”, *Journal of Physics: Condensed Matter* **28**, 293001 (2016).
- ¹⁸B. Bhushan and A. V. Kulkarni, “Effect of normal load on microscale friction measurements”, *Thin Solid Films* **278**, 49–56 (1996).
- ¹⁹B. P. Hung, P. Y. Huri, J. P. Temple, A. Dorafshar, and W. L. Grayson, “Chapter 10 - craniomaxillofacial bone”, in *3d bioprinting and nanotechnology in tissue engineering and regenerative medicine*, edited by L. G. Zhang, J. P. Fisher, and K. W. Leong (Academic Press, 2015), pp. 215–230.

- ²⁰J. Gao, W. D. Luedtke, D. Gourdon, M. Ruths, J. N. Israelachvili, and U. Landman, “Frictional forces and amontons’ law: from the molecular to the macroscopic scale”, *The Journal of Physical Chemistry B* **108**, Publisher: American Chemical Society, 3410–3425 (2004).
- ²¹J. H. Dieterich, “Time-dependent friction in rocks”, *Journal of Geophysical Research (1896-1977)* **77**, 3690–3697 (1972).
- ²²R. Burridge and L. Knopoff, “Model and theoretical seismicity”, *Bulletin of the Seismological Society of America* **57**, 341–371 (1967).
- ²³O. M. Braun and J. Röder, “Transition from stick-slip to smooth sliding: an earthquakelike model”, *Phys. Rev. Lett.* **88**, 096102 (2002).
- ²⁴W. I. Newman and A. M. Gabrielov, “Failure of hierarchical distributions of fibre bundles. I”, *International Journal of Fracture* **50**, 1–14 (1991).
- ²⁵R. F. Smalley Jr., D. L. Turcotte, and S. A. Solla, “A renormalization group approach to the stick-slip behavior of faults”, *Journal of Geophysical Research: Solid Earth* **90**, 1894–1900 (1985).
- ²⁶P. Selvadurai, P. Galvez, P. Mai, and S. Glaser, “Modeling frictional precursory phenomena using a wear-based rate- and state-dependent friction model in the laboratory”, *Tectonophysics* **847**, 229689 (2023).
- ²⁷Y. Mo, K. T. Turner, and I. Szlufarska, “Friction laws at the nanoscale”, *Nature* **457**, 1116–1119 (2009).
- ²⁸G. Carbone and F. Bottiglione, “Asperity contact theories: do they predict linearity between contact area and load?”, *Journal of the Mechanics and Physics of Solids* **56**, 2555–2572 (2008).
- ²⁹F. Bowden and D. Tabor, *The friction and lubrication of solids*, International series of monographs on physics vb. 1 (Clarendon Press, 2001).
- ³⁰H.-J. Kim and D.-E. Kim, “Molecular dynamics simulation of atomic-scale frictional behavior of corrugated nano-structured surfaces”, *Nanoscale* **4**, 3937–3944 (2012).
- ³¹W. Commons, *File:asperities.svg — wikimedia commons, the free media repository*, [Online; accessed 3-February-2023], 2022.
- ³²I. Szlufarska, M. Chandross, and R. W. Carpick, “Recent advances in single-asperity nanotribology”, *Journal of Physics D: Applied Physics* **41**, 123001 (2008).
- ³³G. Binnig, C. F. Quate, and C. Gerber, “Atomic force microscope”, *Phys. Rev. Lett.* **56**, 930–933 (1986).
- ³⁴S. S. Perry, “Scanning Probe Microscopy Measurements of Friction”, *MRS Bulletin* **29**, 478–483 (2004).
- ³⁵Hertz, “On the contact of elastic solids”, *Crelle’s Journal* **92**, 156–171.
- ³⁶D. Maugis, “Adhesion of spheres: the jkr-dmt transition using a dugdale model”, *Journal of Colloid and Interface Science* **150**, 243–269 (1992).
- ³⁷M. H. Müser, “Rigorous field-theoretical approach to the contact mechanics of rough elastic solids”, *Phys. Rev. Lett.* **100**, 055504 (2008).
- ³⁸B. N. J. Persson, “Theory of rubber friction and contact mechanics”, *The Journal of Chemical Physics* **115**, 3840–3861 (2001).
- ³⁹J. A. Greenwood and J. B. P. Williamson, *Contact of nominally flat surfaces*, en, 1966.
- ⁴⁰A. Bush, R. Gibson, and T. Thomas, “The elastic contact of a rough surface”, *Wear* **35**, 87–111 (1975).
- ⁴¹B. Luan and M. O. Robbins, “The breakdown of continuum models for mechanical contacts”, *Nature* **435**, 929–932 (2005).
- ⁴²Y. Dong, A. Vadakkepatt, and A. Martini, “Analytical models for atomic friction”, *Tribology Letters* **44**, 10.1007/s11249-011-9850-2 (2011).
- ⁴³E. Gnecco, R. Bennewitz, T. Gyalog, C. Loppacher, M. Bammerlin, E. Meyer, and H.-J. Güntherodt, “Velocity dependence of atomic friction”, *Phys. Rev. Lett.* **84**, 1172–1175 (2000).
- ⁴⁴P. Hänggi, P. Talkner, and M. Borkovec, “Reaction-rate theory: fifty years after kramers”, *Rev. Mod. Phys.* **62**, 251–341 (1990).
- ⁴⁵Y. Sang, M. Dubé, and M. Grant, “Thermal effects on atomic friction”, *Phys. Rev. Lett.* **87**, 174301 (2001).

- ⁴⁶S. Y. Krylov, K. B. Jinesh, H. Valk, M. Dienwiebel, and J. W. M. Frenken, “Thermally induced suppression of friction at the atomic scale”, *Phys. Rev. E* **71**, 065101 (2005).
- ⁴⁷S. Krylov and J. Frenken, “Thermal contact delocalization in atomic scale friction: a multitude of friction regimes”, English, *New Journal of Physics* **9**, 10.1088/1367-2630/9/10/398 (2007).
- ⁴⁸K. B. Jinesh, S. Y. Krylov, H. Valk, M. Dienwiebel, and J. W. M. Frenken, “Thermolubricity in atomic-scale friction”, *Phys. Rev. B* **78**, 155440 (2008).
- ⁴⁹M. H. Müser, “Nature of mechanical instabilities and their effect on kinetic friction”, *Phys. Rev. Lett.* **89**, 224301 (2002).
- ⁵⁰Q. Li, Y. Dong, D. Perez, A. Martini, and R. W. Carpick, “Speed dependence of atomic stick-slip friction in optimally matched experiments and molecular dynamics simulations”, *Phys. Rev. Lett.* **106**, 126101 (2011).
- ⁵¹Y. Dong, Q. Li, and A. Martini, “Molecular dynamics simulation of atomic friction: a review and guide”, *Journal of Vacuum Science & Technology A* **31**, 030801 (2013).
- ⁵²K. Johnson and J. Woodhouse, “Stick-slip motion in the atomic force microscope”, *Tribology Letters* **5**, 155–160 (1998).
- ⁵³S. N. Medyanik, W. K. Liu, I.-H. Sung, and R. W. Carpick, “Predictions and observations of multiple slip modes in atomic-scale friction”, *Phys. Rev. Lett.* **97**, 136106 (2006).
- ⁵⁴A. Vanossi, N. Manini, M. Urbakh, S. Zapperi, and E. Tosatti, “Modeling friction: from nanoscale to mesoscale”, *Reviews of Modern Physics* **85**, 529–552 (2013).
- ⁵⁵J. Frenkel and T. Kontorova, “On the theory of plastic deformation and twinning”, *Phys. Z. Soviet.* **13** (1938).
- ⁵⁶J. Norell, A. Fasolino, and A. Wijn, “Emergent friction in two-dimensional frenkel-kontorova models”, *Physical Review E* **94**, 10.1103/PhysRevE.94.023001 (2016).
- ⁵⁷M. Dienwiebel, N. Pradeep, G. S. Verhoeven, H. W. Zandbergen, and J. W. Frenken, “Model experiments of superlubricity of graphite”, *Surface Science* **576**, 197–211 (2005).
- ⁵⁸C. Kittel, *Introduction to solid state physics*, 8th ed. (Wiley, 2004).
- ⁵⁹J. A. van den Ende, A. S. de Wijn, and A. Fasolino, “The effect of temperature and velocity on superlubricity”, *Journal of Physics: Condensed Matter* **24**, 445009 (2012).
- ⁶⁰M. Weiss and F.-J. Elmer, “Dry friction in the Frenkel-Kontorova-Tomlinson model: dynamical properties”, *Zeitschrift für Physik B Condensed Matter* **104**, 55–69 (1997).
- ⁶¹B. Bhushan, “Nanotribology and nanomechanics”, *Wear* **259**, 15th International Conference on Wear of Materials, 1–? (2005).
- ⁶²O. Penkov, H.-J. Kim, H.-J. Kim, and D.-E. Kim, “Tribology of graphene: A review”, *International Journal of Precision Engineering and Manufacturing* **15**, 577–585 (2014).
- ⁶³X. Zhao, M. Hamilton, W. G. Sawyer, and S. S. Perry, “Thermally activated friction”, *Tribology Letters* **27**, 113–117 (2007).
- ⁶⁴G Paolicelli, M Tripathi, V Corradini, A Candini, and S Valeri, “Nanoscale frictional behavior of graphene on sio₂ and ni(111) substrates”, *Nanotechnology* **26**, 055703 (2015).
- ⁶⁵S. Zhang, Y. Hou, S. Li, L. Liu, Z. Zhang, X.-Q. Feng, and Q. Li, “Tuning friction to a superlubric state via in-plane straining”, *Proceedings of the National Academy of Sciences* **116**, Publisher: Proceedings of the National Academy of Sciences, 24452–24456 (2019).
- ⁶⁶M. R. Vazirisereshk, H. Ye, Z. Ye, A. Otero-de-la Roza, M.-Q. Zhao, Z. Gao, A. T. C. Johnson, E. R. Johnson, R. W. Carpick, and A. Martini, “Origin of nanoscale friction contrast between supported graphene, mos₂, and a graphene/mos₂ heterostructure”, *Nano Letters* **19**, PMID: 31267757, 5496–5505 (2019).
- ⁶⁷H. M. Yoon, Y. Jung, S. C. Jun, S. Kondaraju, and J. S. Lee, “Molecular dynamics simulations of nanoscale and sub-nanoscale friction behavior between graphene and a silicon tip: analysis of tip apex motion.”, *Nanoscale* **7** **14**, 6295–303 (2015).
- ⁶⁸S. Li, Q. Li, R. W. Carpick, P. Gumbsch, X. Z. Liu, X. Ding, J. Sun, and J. Li, “The evolving quality of frictional contact with graphene”, *Nature* **539**, Number: 7630, 541–545 (2016).

- ⁶⁹A. Wijn, A. Fasolino, A. Filippov, and M. Urbakh, “Low friction and rotational dynamics of crystalline flakes in solid lubrication”, *Europhysics Letters (epl)* **95**, 10.1209/0295-5075/95/66002 (2011).
- ⁷⁰X. Feng, S. Kwon, J. Y. Park, and M. Salmeron, “Superlubric sliding of graphene nanoflakes on graphene”, *ACS Nano* **7**, Publisher: American Chemical Society, 1718–1724 (2013).
- ⁷¹F. Bonelli, N. Manini, E. Cadelano, and L. Colombo, “Atomistic simulations of the sliding friction of graphene flakes”, *The European Physical Journal B* **70**, 449–459 (2009).
- ⁷²M. Reguzzoni, A. Fasolino, E. Molinari, and M. C. Righi, “Friction by shear deformations in multilayer graphene”, *The Journal of Physical Chemistry C* **116**, 21104–21108 (2012).
- ⁷³Y. Liu, F. Grey, and Q. Zheng, “The high-speed sliding friction of graphene and novel routes to persistent superlubricity”, *Scientific Reports* **4**, 4875 (2014).
- ⁷⁴P. Zhu and R. Li, “Study of nanoscale friction behaviors of graphene on gold substrates using molecular dynamics”, *Nanoscale Research Letters* **13**, 34 (2018).
- ⁷⁵J. Zhang, E. Osloub, F. Siddiqui, W. Zhang, T. Ragab, and C. Basaran, “Anisotropy of graphene nanoflake–diamond interface frictional properties”, *Materials* **12**, 10.3390/ma12091425 (2019).
- ⁷⁶A. Sircar and P. K. Patra, “A simple generalization of Prandtl–Tomlinson model to study nanoscale rolling friction”, *Journal of Applied Physics* **127**, 135102, 10.1063/1.5143062 (2020).
- ⁷⁷M. Reguzzoni and M. C. Righi, “Size dependence of static friction between solid clusters and substrates”, *Phys. Rev. B* **85**, 201412 (2012).
- ⁷⁸N. Varini, A. Vanossi, R. Guerra, D. Mandelli, R. Capozza, and E. Tosatti, “Static friction scaling of physisorbed islands: the key is in the edge”, *Nanoscale* **7**, 2093–2101 (2015).
- ⁷⁹T. Fileteer, J. L. McChesney, A. Bostwick, E. Rotenberg, K. V. Emtsev, T. Seyller, K. Horn, and R. Bennewitz, “Friction and dissipation in epitaxial graphene films”, *Phys. Rev. Lett.* **102**, 086102 (2009).
- ⁸⁰C. Lee, Q. Li, W. Kalb, X. Liu, H. Berger, R. Carpick, and J. Hone, “Frictional characteristics of atomically thin sheets”, *Science (New York, N.Y.)* **328**, 76–80 (2010).
- ⁸¹E. Thormann, “Negative friction coefficients”, *Nature Materials* **12**, 468–468 (2013).
- ⁸²O Zwörner, H Hölscher, U. Schwarz, and R Wiesendanger, “The velocity dependence of frictional forces in point-contact friction”, *APPLIED PHYSICS A MATERIALS SCIENCE AND PROCESSING* **66**, S263–S268 (1998).
- ⁸³R. Guerra, U. Tartaglino, A. Vanossi, and E. Tosatti, “Ballistic nanofriction”, *Nature Materials* **9**, 634–637 (2010).
- ⁸⁴H. Tomaç, Z. Guchan, and N. Altun, “How the stiletto heeled shoes which are popularly preferred by many women affect balance and functional skills?”, *Health Care for Women International* **43**, 1–11 (2020).
- ⁸⁵K. Gibbs, *Pressure*, (2020) https://www.schoolphysics.co.uk/age16-19/Mechanics/Statics/text/Pressure_index.html.
- ⁸⁶F. B. Ltd, *Foot facts*, (2023) <https://www.footbionics.com/Patients/Foot+Facts.html>.